AGU PUBLICATIONS

Journal of Advances in Modeling Earth Systems

RESEARCH ARTICLE

10.1002/2013MS000278

Key Points:
- ITCZ diabatic heating and Ekman pumping are studied using an analytical model
- Deep diabatic heating in the inviscid interior forces a deep Hadley circulation
- Ekman boundary layer pumping forces a shallow Hadley circulation

Correspondence to:
A. O. Gonzalez,
gonzalez@atmos.colostate.edu

Citation:
Gonzalez, A. O., and G. Mora Rojas (2014), Balanced dynamics of deep and shallow Hadley circulations in the tropics, *J. Adv. Model. Earth Syst.*, *06*, doi:10.1002/2013MS000278.

Received 1 NOV 2013
Accepted 29 APR 2014
Accepted article online 6 MAY 2014

Balanced dynamics of deep and shallow Hadley circulations in the tropics

Alex O. Gonzalez[1] and Gabriela Mora Rojas[1]

[1]Department of Atmospheric Science, Colorado State University, Fort Collins, Colorado, USA

Abstract This paper examines the dynamics of large-scale overturning circulations in the tropical atmosphere using an idealized zonally symmetric model on the equatorial β-plane. Under certain simplifications of its coefficients, the elliptic partial differential equation for the transverse circulation can be solved by first performing a vertical transform to obtain a horizontal structure equation, and then using Green's function to solve the horizontal structure equation. When deep diabatic heating is present in the Intertropical Convergence Zone (ITCZ), the deep Hadley circulation is of first-order importance. In the absence of deep diabatic heating, the interior circulation associated with Ekman pumping cannot penetrate deep into the troposphere because the resistance of fluid parcels to horizontal motion (i.e., inertial stability) is significantly smaller than their resistance to vertical motion (i.e., static stability). In this scenario, only a shallow Hadley circulation exists. The shallow overturning circulation is characterized by meridional velocities as large as 7 m s^{-1} at the top of the boundary layer, in qualitative agreement with observations in the tropical eastern Pacific. The meridional asymmetry between the winter and summer deep and shallow Hadley cells is attributed to the anisotropy of the inertial stability parameter, and as the ITCZ widens meridionally or as the forcing involves higher vertical wave numbers, the asymmetry between the winter and summer cells increases.

1. Introduction

Zhang et al. [2004] have presented comprehensive observations of shallow meridional overturning circulations in the tropical eastern Pacific. As illustrated in Figure 1, this shallow overturning circulation resembles the deep Hadley circulation in many respects, but its cross-equatorial return flow is located just above the top of the boundary layer instead of just below the tropopause. *Schneider and Lindzen* [1977], *Tomas and Webster* [1997], and *Trenberth et al*. [2000] emphasized the importance of shallow overturning circulations in the tropics before the observations in *Zhang et al*. [2004].

Schneider and Lindzen [1977] illustrated a large-scale overturning circulation confined below 800 hPa forced by a zonally symmetric sea surface temperature (SST) distribution. They explain that the circulation is confined to the boundary layer due to the vertical variation of small-scale turbulent mixing that they assumed. *Tomas and Webster* [1997] suggested that a shallow divergent circulation exists in all tropical ocean basins, but is most prominent in basins such as the eastern Pacific, where cross-equatorial SST gradients are strongest. They describe the shallow overturning circulation as a secondary circulation that acts to advect absolute vorticity across the equator, allowing the Intertropical Convergence Zone (ITCZ) to form off of the equator. *Trenberth et al*. [2000] performed an Empirical Orthogonal Function (EOF) analysis on the divergent part of the tropical wind field in the National Centers for Environmental Prediction-National Center for Atmospheric Research (NCEP-NCAR) and European Centre for Medium-Range Weather Forecasts (ECMWF) global model reanalysis products in the tropics. The first EOF mode represented deep overturning circulations, while the second EOF mode represented shallow overturning circulations. Shallow overturning circulations were present in the eastern Pacific, west Africa, the Atlantic, North America, and South America. *Yin and Albrecht* [2000] also provided observations of shallow overturning circulations in the eastern Pacific (90°−150°W) using the First Global Atmospheric Research Program (GARP) Global Experiment (FGGE) dropsonde sounding data.

Motivated by the observations of *Zhang et al*. [2004], *Nolan et al*. [2007] interpreted the shallow overturning circulation in the eastern Pacific as a large-scale sea breeze circulation, driven by anomalously large north-south SST gradients when deep convection is absent in the ITCZ. The ITCZ of the eastern Pacific is an area

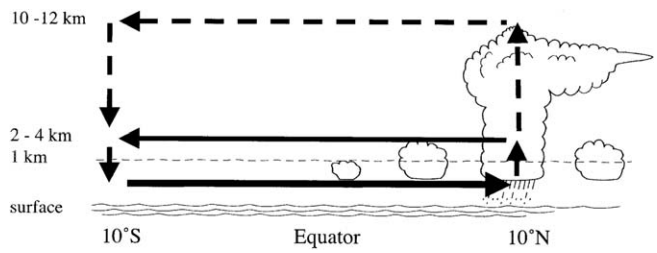

Figure 1. Schematic cross section of the deep (dashed lines) and shallow (solid lines) meridional circulations in the tropical eastern Pacific. Adapted from *Zhang et al.* [2004, Figure 1], © American Meteorological Society, and used with permission.

of relatively low surface pressure and warm SSTs compared to the area near and just south of the equator, leading to a cross-equatorial southerly flow in the boundary layer. The ITCZ region has larger thicknesses between pressure levels since it is warmer, which leads to a reversal in the meridional pressure gradient and an associated shallow northerly return flow just above the boundary layer. Equatorial regions with significant large-scale cold tongues, such as the eastern Pacific, and coastal regions with land-ocean contrasts, such as west Africa, exhibit large enough surface temperature gradients to have this meridional pressure gradient reversal. *Zhang et al.* [2008] classify shallow overturning circulations into two types: (i) the maritime ITCZ type (e.g., the eastern Pacific) and (ii) the summer monsoon type (e.g., west Africa). They also note that shallow overturning circulations have a seasonal cycle, can be located on either side of the ITCZ, and have distinct vertical structures.

The purpose of the present paper is to discuss several other dynamical aspects, which, in addition to surface temperature gradients, appear to play an important role in understanding shallow overturning circulations. The main dynamical aspects discussed here are: (i) diabatic heating in the inviscid interior of the ITCZ; (ii) Ekman pumping out of the boundary layer in the high positive vorticity region of the ITCZ; and (iii) low inertial stability in the equatorial region, causing the winter Hadley cell to be stronger than the summer cell in response to both diabatic and frictional forcings.

Such ideas are similar to those considered by *Schubert and McNoldy* [2010], who studied Ekman pumping at the top of the boundary layer in tropical cyclones. They illustrated the existence of shallow overturning circulations with return flow just above the top of the boundary layer in tropical cyclones of varying strengths using an axisymmetric model on the *f*-plane. The analogous model in the ITCZ is a zonally symmetric model on the equatorial β-plane, which will be used in this study.

As we will see, the zonally symmetric model equations help explain both shallow overturning circulations and the deep Hadley circulation, therefore they are useful in discussing both circulations in the context of one theory of large-scale flows in the ITCZ. There are two schools of thought in modeling flows in the ITCZ. The first involves an assumption of monthly or longer time scales, as shown by *Schneider and Lindzen* [1977], *Held and Hou* [1980], *Lindzen and Hou* [1988], and *Hou and Lindzen* [1992]. The model used in this study focuses on the second school of thought, in which the zonal velocity and temperature fields are transient, as explored by *Hack et al.* [1989], *Hack and Schubert* [1990], *Nieto Ferreira and Schubert* [1997], and *Wang and Magnusdottir* [2005]. If the zonal flow is balanced in the sense that it is continuously evolving from one geostrophically balanced state to another, then the meridional circulation is determined by the solution of a second-order partial differential equation in the (y, z)-plane [*Eliassen*, 1951]. According to this "meridional circulation equation," the stream function for the meridional and vertical motion in the inviscid interior is forced by the meridional derivative of the diabatic heating and the Ekman pumping, and is shaped by the static stability, baroclinicity, and inertial stability. Although solutions of the meridional circulation equation generally yield meridional and vertical velocities that are much weaker than the zonal velocity, the meridional and vertical directions are the directions of large gradients, so the relatively weak meridional circulation is crucial for the temporal evolution of the zonal flow.

The paper is organized in the following way. In section 2, the balanced zonally symmetric model and the associated meridional circulation equation are presented. Section 3 introduces a vertical transform that converts the meridional circulation equation into a differential equation for the y-structure of the circulation. In section 4, the differential equation in y is solved using the Green's function. Section 5 discusses the deep overturning response associated with diabatic heating in the ITCZ. Section 6 discusses the shallow overturning response due to Ekman pumping at the top of boundary layer in the absence of diabatic heating. In section 7, solutions describing the asymmetry between the winter and summer Hadley cells are presented. Concluding remarks are discussed in section 8.

2. Model Equations

Consider zonally symmetric balanced motions in a stratified and compressible atmosphere on the equatorial β-plane. Only the flow in the inviscid interior (i.e., above the 900 hPa isobaric surface) is explicitly modeled. Frictional effects are represented through the specification of the Ekman pumping at the top of the boundary layer, $z = 0$. This nonzero lower boundary condition will be discussed later in this section. As the vertical coordinate, $z = H\ln(p_0/p)$ is used, where $p_0 = 900$ hPa, $T_0 = 293$ K, and $H = RT_0/g = 8581$ m. This study considers the case of weak horizontal flow and weak baroclinicity (i.e., the $v(\partial u/\partial y)$ and $w(\partial u/\partial z)$ terms in the zonal momentum equation and the $v(\partial T/\partial y)$ term in the thermodynamic equation are neglected). These simplifications allow us to construct analytical solutions of the problem. As will be seen, these analytical results agree well with the numerical results obtained by *Hack et al.* [1989], who did not assume weak horizontal flow and weak baroclinicity and whose elliptic equation coefficients for static stability, baroclinicity, and inertial stability do not contain approximations.

Under these assumptions, the governing equations for balanced zonal flow are of the form

$$\frac{\partial u}{\partial t} - \beta y v = 0, \tag{1}$$

$$\beta y u + \frac{\partial \phi}{\partial y} = 0, \tag{2}$$

$$\frac{\partial \phi}{\partial z} = \frac{g}{T_0} T, \tag{3}$$

$$\frac{\partial v}{\partial y} + \frac{\partial w}{\partial z} - \frac{w}{H} = 0, \tag{4}$$

$$\frac{\partial T}{\partial t} + \frac{T_0}{g} N^2 w = \frac{Q}{c_p}, \tag{5}$$

where u and v are the zonal and meridional components of velocity, w is the log-pressure vertical velocity, ϕ is the perturbation geopotential, T is the perturbation temperature, $\beta = 2\Omega/a$ is the constant northward gradient of the Coriolis parameter, Ω and a are the Earth's rotation rate and radius, Q is the diabatic heating, and $N^2(z) = (g/T_0)[(d\bar{T}/dz) + (\kappa\bar{T}/H)]$ is the square of the buoyancy frequency, which is computed from the specified mean temperature profile $\bar{T}(z)$. Equations (1–5) constitute a system of five equations in the six unknowns u, v, w, ϕ, T, Q, so an additional "parameterization" relating Q to the other unknowns is required for closure. In order to simplify the problem, Q will be prescribed.

Equations (1–5) can be combined in such a way as to obtain a single equation for the stream function of the meridional overturning circulation. We begin the derivation by multiplying the zonal wind equation (1) by βy and the thermodynamic equation (5) by (g/T_0), and we make use of the geostrophic equation (2) and the hydrostatic equation (3), thereby obtaining

$$\frac{\partial}{\partial y}\left(\frac{\partial \phi}{\partial t}\right) + \beta^2 y^2 v = 0, \tag{6}$$

$$\frac{\partial}{\partial z}\left(\frac{\partial \phi}{\partial t}\right) + N^2 w = \frac{g}{c_p T_0} Q. \tag{7}$$

Eliminating $(\partial\phi/\partial t)$ between (6) and (7) results in

$$N^2 \frac{\partial w}{\partial y} - \beta^2 y^2 \frac{\partial v}{\partial z} = \frac{g}{c_p T_0}\frac{\partial Q}{\partial y}. \tag{8}$$

Equations (4) and (8) can now be regarded as a closed system in v and w. One way of proceeding from this system is to make use of (4) so that the meridional circulation (v, w) can be expressed in terms of the stream function ψ. The formulas that relate (v, w) and ψ are

$$e^{-z/H}v = -\frac{\partial\psi}{\partial z} \quad \text{and} \quad e^{-z/H}w = \frac{\partial\psi}{\partial y}. \tag{9}$$

In order to obtain a single equation in $\psi(y,z,t)$, we substitute (9) into (8). This procedure yields the partial differential equation given below in (10). Assuming that $v \to 0$ as $y \to \pm\infty$ and that w vanishes at the top boundary ($z = z_T$), the boundary conditions given below in (11) and (12) are obtained. Since this study is concerned with Ekman pumping effects on the fluid interior, the actual vertical velocity (i.e., the physical height vertical velocity) is specified at the lower isobaric surface $z = 0$. Even though the lower boundary condition should be applied at a fixed physical height, *Haynes and Shepherd* [1989] suggest that the errors associated with assuming a value for the physical height vertical velocity on an isobaric lower boundary are minor compared to those associated with assuming a value for the log-pressure (or just pressure) vertical velocity on an isobaric lower boundary. The appropriate linearized version of the lower boundary condition used here is

$$\frac{\partial\phi}{\partial t} + g\frac{\partial\psi}{\partial y} = g\mathcal{W} \text{ at } z=0,$$

where $\mathcal{W}(y,t)$ is the specified physical height vertical velocity at $z = 0$. Equation (6) must be used to eliminate $(\partial\phi/\partial t)$ and thereby express the lower boundary condition in terms of the stream function. From (6),

$$\frac{\partial}{\partial y}\left(\frac{\partial\phi}{\partial t}\right) - \beta^2 y^2 \frac{\partial\psi}{\partial z} = 0 \text{ at } z=0.$$

Eliminating $(\partial\phi/\partial t)$ from these last two relations, we obtain the lower boundary condition given below in (13). In summary, the meridional circulation problem is

$$N^2 e^{z/H}\frac{\partial^2\psi}{\partial y^2} + \beta^2 y^2 \frac{\partial}{\partial z}\left(e^{z/H}\frac{\partial\psi}{\partial z}\right) = \frac{g}{c_p T_0}\frac{\partial Q}{\partial y}. \tag{10}$$

with boundary conditions

$$\psi \to 0 \text{ as } y \to \pm\infty, \tag{11}$$

$$\psi = 0 \text{ at } z = z_T, \tag{12}$$

$$g\frac{\partial^2\psi}{\partial y^2} + \beta^2 y^2 \frac{\partial\psi}{\partial z} = g\frac{\partial\mathcal{W}}{\partial y} \text{ at } z=0. \tag{13}$$

Note that the diabatic forcing appears through the right-hand side of the interior equation (10), while the Ekman pumping appears through the right-hand side of the lower boundary condition (13). Also, note that N^2 is a measure of the static stability and $\beta^2 y^2$ is a measure of the inertial stability, which both act as shaping parameters. Baroclinicity is also a shaping parameter, but it does not appear because of the simplifications introduced in (1–5).

The meridional circulation problem (10–13) can be written in a slightly simpler form by defining $\hat{\psi}(y,z,t)$ and $\hat{Q}(y,z,t)$ as

$$\begin{aligned} \hat{\psi}(y,z,t) &= \psi(y,z,t)e^{z/2H}, \\ \hat{Q}(y,z,t) &= Q(y,z,t)e^{-z/2H}. \end{aligned} \tag{14}$$

Using (14) in (10–13) the diagnostic problem is written in the form

$$N^2\frac{\partial^2\hat{\psi}}{\partial y^2} + \beta^2 y^2\left(\frac{\partial^2\hat{\psi}}{\partial z^2} - \frac{\hat{\psi}}{4H^2}\right) = \frac{g}{c_p T_0}\frac{\partial\hat{Q}}{\partial y}, \tag{15}$$

with boundary conditions

$$\hat{\psi} \to 0 \text{ as } y \to \pm\infty, \tag{16}$$

$$\hat{\psi}=0 \text{ at } z=z_T, \tag{17}$$

$$g\frac{\partial^2\hat{\psi}}{\partial y^2}+\beta^2 y^2\left(\frac{\partial\hat{\psi}}{\partial z}-\frac{\hat{\psi}}{2H}\right)=g\frac{\partial\mathcal{W}}{\partial y} \text{ at } z=0. \tag{18}$$

Note that (15) has a convenient form because of the absence of the $e^{z/H}$ factors. The elliptic problem (15–18) indicates that the meridional circulation is forced by the y-derivative of the interior diabatic heating, $\partial\hat{Q}/\partial y$, and by the y-derivative of the Ekman pumping, $\partial\mathcal{W}/\partial y$, and is shaped by the static stability N^2 and the inertial stability $\beta^2 y^2$. Because of the linearity of the problem and the associated superposition principle, the two forcing effects will be treated separately, with deep diabatic heating discussed in section 5, and the upward penetration of Ekman pumping discussed in section 6.

3. Vertical Transform of the Meridional Circulation Equation

Solutions of (15–18) are computed via the vertical transform pair

$$\hat{\psi}(y,z,t)=\sum_{m=0}^{\infty}\hat{\psi}_m(y,t)\mathcal{Z}_m(z), \tag{19}$$

$$\hat{\psi}_m(y,t)=\frac{1}{g}\int_0^{z_T}\hat{\psi}(y,z,t)\mathcal{Z}_m(z)N^2(z)dz+\hat{\psi}(y,0,t)\mathcal{Z}_m(0). \tag{20}$$

In other words, the stream function $\hat{\psi}(y,z,t)$ is represented in terms of a series of vertical structure functions $\mathcal{Z}_m(z)$, with the coefficients $\hat{\psi}_m(y,t)$ given by (20), where m refers to the vertical modes. The reason for the last term in (20) arises from the lower boundary condition (18), as will become apparent shortly. The vertical structure functions $\mathcal{Z}_m(z)$ are solutions of the Sturm-Liouville eigenvalue problem

$$\frac{d^2\mathcal{Z}_m}{dz^2}-\frac{\mathcal{Z}_m}{4H^2}=-\frac{N^2\mathcal{Z}_m}{gh_m}, \tag{21}$$

$$\mathcal{Z}_m=0 \text{ at } z=z_T, \tag{22}$$

$$\frac{d\mathcal{Z}_m}{dz}-\frac{\mathcal{Z}_m}{2H}=-\frac{\mathcal{Z}_m}{h_m} \text{ at } z=0, \tag{23}$$

with eigenvalues (or equivalent depths) denoted by h_m. These equivalent depths correspond to the solution of the Sturm-Liouville eigenvalue problem (21–23), where the eigenfunctions are denoted by $\mathcal{Z}_m(z)$. For $N^2(z)>0$, the solutions of the Sturm-Liouville problem have the following three properties [*Fulton and Schubert*, 1985]: (i) The eigenvalues h_m are real and may be ordered such that $h_0>h_1>\cdots h_m>0$ with $h_m\to 0$ as $m\to\infty$; (ii) The eigenfunctions $\mathcal{Z}_m(z)$ are orthogonal and may be chosen to be real; and (iii) the eigenfunctions $\mathcal{Z}_m(z)$ form a complete set. A discussion of the transform pair (19 and 20) is given in Appendix , along with a proof of properties (i) and (ii). The derivation of the solutions to the eigenvalue problem (21–23) for the special case of constant N as well as a proof of property (iii) are given in Appendix A. The first five vertical structure functions $\mathcal{Z}_m(z)$ for the special case of constant N are plotted in Figure 2.

To take the vertical transform of (15), we multiply it by $\mathcal{Z}_m(z)$ and integrate in z from 0 to z_T to yield

$$\begin{aligned}\frac{\partial^2}{\partial y^2}\int_0^{z_T}\hat{\psi}(y,z,t)\mathcal{Z}_m(z)N^2(z)dz+\beta^2y^2\left[\mathcal{Z}_m(z)\frac{\partial\hat{\psi}(y,z,t)}{\partial z}-\hat{\psi}(y,z,t)\frac{d\mathcal{Z}_m(z)}{dz}\right]_0^{z_T}\\ +\beta^2y^2\int_0^{z_T}\hat{\psi}(y,z,t)\left(\frac{d^2\mathcal{Z}_m(z)}{dz^2}-\frac{\mathcal{Z}_m(z)}{4H^2}\right)dz=\frac{g}{c_pT_0}\frac{\partial}{\partial y}\int_0^{z_T}\hat{Q}(y,z,t)\mathcal{Z}_m(z)dz.\end{aligned} \tag{24}$$

Note that the integral originating from $\beta^2y^2(\partial^2\hat{\psi}/\partial z^2)$ in (15) is integrated by parts twice. In order to simplify (24), we use (21) in the third line and then use (17) and (22) to show that the upper boundary term in the second line vanishes. To evaluate the lower boundary term in the second line, we eliminate $\partial\hat{\psi}/\partial z$ by using (18) and

then group the resulting $\partial^2\hat{\psi}/\partial y^2$ term with the first line of (24). Similarly, we use (23) to eliminate $d\mathcal{Z}_m/dz$ and then group the resulting $\mathcal{Z}_m/h_m$ term with the third line of (24). This procedure simplifies (24) to

$$\begin{aligned} & \frac{\partial^2}{\partial y^2}\left[\frac{1}{g}\int_0^{z_T}\hat{\psi}(y,z,t)\mathcal{Z}_m(z)N^2(z)dz+\hat{\psi}(y,0,t)\mathcal{Z}_m(0)\right] \\ - & \frac{\beta^2 y^2}{gh_m}\left[\frac{1}{g}\int_0^{z_T}\hat{\psi}(y,z,t)\mathcal{Z}_m(z)N^2(z)dz+\hat{\psi}(y,0,t)\mathcal{Z}_m(0)\right] \\ = & \frac{\partial}{\partial y}\left[\int_0^{z_T}\frac{\hat{Q}(y,z,t)}{c_pT_0}\mathcal{Z}_m(z)dz+\mathcal{W}(y,t)\mathcal{Z}_m(0)\right]. \end{aligned} \tag{25}$$

Then, with the use of (20), the meridional structure equation becomes

$$\frac{\partial^2\hat{\psi}_m(y,t)}{\partial y^2}-\frac{y^2}{4b_m^4}\hat{\psi}_m(y,t)=\frac{\partial F_m(y,t)}{\partial y}, \tag{26}$$

with boundary conditions

$$\hat{\psi}_m(y,t)\to 0 \text{ as } y\to\pm\infty, \tag{27}$$

where the forcing term $F_m(y,t)$ on the right-hand side of (26) is given by

$$F_m(y,t)=\int_0^{z_T}\frac{\hat{Q}(y,z,t)}{c_pT_0}\mathcal{Z}_m(z)dz+\mathcal{W}(y,t)\mathcal{Z}_m(0), \tag{28}$$

and where the equatorial Rossby length b_m is given by

$$b_m=\left(\frac{gh_m}{4\beta^2}\right)^{1/4}=\varepsilon_m^{-1/4}\frac{a}{\sqrt{2}}. \tag{29}$$

Lamb's parameter is defined by $\varepsilon_m = 4\Omega^2a^2/(gh_m)$. The spectra of equivalent depths h_m, equatorial Rossby lengths b_m, and Lamb's parameters ε_m for $m = 0,1,2, \ldots, 10$ are shown in Table 1. Note that the interior diabatic heating $\hat{Q}(y,z,t)$ and the boundary layer pumping $\mathcal{W}(y,t)$, which were separate forcing effects in (15) and (18), have now merged into the single forcing term $F_m(y,t)$.

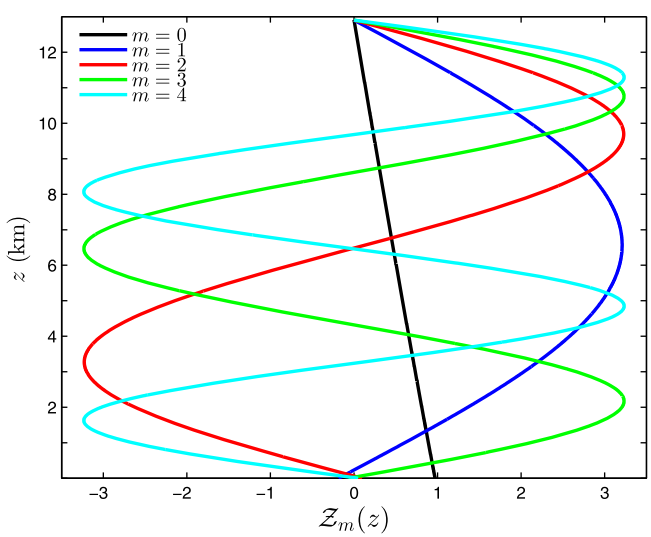

Figure 2. Vertical structure functions $\mathcal{Z}_m(z)$ for the external mode $m = 0$ and the first four internal modes $m = 1, 2, 3, 4$. As discussed in Appendix , these vertical structure functions are solutions of the Sturm-Liouville problem (21–23) with the constant buoyancy frequency $N = 1.2 \times 10^{-2}\ \mathrm{s}^{-1}$ and $z_T = 13$ km.

4. Solution of the Horizontal Structure Equation Via the Green's Function

In order to solve (26) and (27), the Green's function $G_m(y,y')$ is introduced, which is the solution of the ordinary differential equation

$$\frac{d^2G_m}{dy^2}-\frac{y^2}{4b_m^4}G_m=-\frac{1}{b_m^2}\delta\left(\frac{y-y'}{b_m}\right), \tag{30}$$

with the boundary conditions

Table 1. Information About the First 11 Vertical Wave Numbers[a]

m	h_m (m)	$(gh_m)^{1/2}$ (m s^{-1})	b_m (km)	ϵ_m
0	7099	263.8 (—–)	2400	12.41
1	229.8	47.46 (48.27)	1018	383.4
2	61.42	24.53 (24.65)	732.0	1434
3	27.66	16.46 (16.50)	599.7	3185
4	15.63	12.38 (12.39)	519.9	5636
5	10.03	9.912 (9.920)	465.3	8787
6	6.970	8.265 (8.270)	424.9	12,638
7	5.125	7.087 (7.090)	393.4	17,190
8	3.925	6.202 (6.204)	368.1	22,442
9	3.103	5.514 (5.515)	347.0	28,394
10	2.514	4.963 (4.964)	329.3	35,046

[a]The spectra of equivalent depths h_m, gravity wave speeds $(gh_m)^{1/2}$ (with approximate values in parentheses), equatorial Rossby lengths $b_m=[gh_m/(4\beta^2)]^{1/4}$, and Lamb's parameters $\epsilon_m=4\Omega^2a^2/(gh_m)$ for the 11 values of m listed in the left column. The values have been computed from (B4) and (B10) using $z_T=13$ km, $g=9.8$ m s^{-2}, $a=6371$ km, $\Omega=7.292\times10^{-5}$s^{-1}, $N=1.2\times10^{-2}$s^{-1}, and $H=8581$ m.

$$G_m(y,y') \to 0 \text{ as } y \to \pm\infty, \tag{31}$$

where the Dirac delta function vanishes for $y \neq y'$ and satisfies

$$\frac{1}{b_m}\int_{y'-}^{y'+}\delta\left(\frac{y-y'}{b_m}\right)dy=1. \tag{32}$$

The Green's function $G_m(y,y')$ is useful in understanding the meridional structure of the Hadley circulation since the left-hand side of (30) is equivalent to that of (26). As will be seen, all of the meridional asymmetry of the Hadley circulation is built into the Green's function. The Green's function $G_m(y,y')$ is constructed from the parabolic cylinder functions $D_\nu(x)$, which satisfy

$$\frac{d^2D_\nu}{dx^2}+\left(\nu+\frac{1}{2}-\frac{1}{4}x^2\right)D_\nu=0. \tag{33}$$

Note that the order $\nu=-1/2$ parabolic cylinder functions $D_{-1/2}(y/b_m)$ and $D_{-1/2}(-y/b_m)$ are solutions of the homogeneous version of (30). The functions $D_{-1/2}(x)$ and $D_{-1/2}(-x)$ are plotted in Figure 3. Only the solution $G_m(y,y')=\alpha_1D_{-1/2}(-y/b_m)$ is valid for $-\infty \leq y \leq y'$, and only the solution $G_m(y,y')=\alpha_2D_{-1/2}(y/b_m)$ is valid for $y' \leq y < \infty$ because of the lateral boundary conditions (31). Note that α_1 and α_2 depend on y', and are determined by requiring that $G_m(y,y')$ is continuous at $y=y'$ and that the jump in the first derivative satisfies

$$b_m\left[\frac{dG_m}{dy}\right]_{y'-}^{y'+}=-1, \tag{34}$$

which is obtained by integrating (30) across a narrow region surrounding $y=y'$, making use of the delta function property (32), and noting that the narrow integral of the first term left of the equals sign in (30) is zero. The two algebraic equations for α_1 and α_2 can be solved with the aid of the Wronskian

$$D_{-1/2}(x)\frac{dD_{-1/2}(-x)}{dx}-D_{-1/2}(-x)\frac{dD_{-1/2}(x)}{dx}=\sqrt{2}. \tag{35}$$

The Wronskian is derived by multiplying (33) by $D_\nu(-x)$ and multiplying the version of (33) where $x \to -x$ by $D_\nu(x)$, and combining the two resulting equations. Solving for α_1 and α_2 using (35) results in

$$G_m(y,y')=\frac{1}{\sqrt{2}}\begin{cases} D_{-1/2}(y'/b_m)D_{-1/2}(-y/b_m) & \text{if } -\infty < y \leq y' \\ D_{-1/2}(-y'/b_m)D_{-1/2}(y/b_m) & \text{if } y' \leq y < \infty. \end{cases} \tag{36}$$

Plots of $G_m(y,y')$ for $y'=-1500, -750, 0, 750, 1500$ km and $m=0, 1, 2$ are shown in Figure 4. Note that, as m increases, the jump in the derivative of $G_m(y,y')$ at $y=y'$ in (34) increases since b_m decreases.

Therefore, the Green's function becomes more confined to the region near $y = y'$ and we expect the response of the Hadley circulation to become more confined in the meridional direction. Also, note the meridional asymmetry of the Green's function between either side of y' when y' is placed away from the equator. Therefore, we expect the Hadley cells to reflect this asymmetry when the ITCZ is placed off of the equator.

To express the solution $\hat{\psi}_m(y,t)$ in terms of the Green's function, we multiply (26) by $G_m(y,y')$, multiply (30) by $\hat{\psi}_m(y,t)$, and then take the difference of the resulting equations to obtain

$$\frac{\partial}{\partial y}\left(G_m(y,y')\frac{\partial\hat{\psi}_m(y,t)}{\partial y}-\hat{\psi}_m(y,t)\frac{dG_m(y,y')}{dy}\right)=\frac{\partial F_m(y,t)}{\partial y}G_m(y,y')+\hat{\psi}_m(y,t)\frac{1}{b_m}\delta\left(\frac{y-y'}{b_m}\right). \tag{37}$$

We now integrate (37) over y, apply the boundary conditions (27) and (31), use the delta function property (32) and the Green's function symmetry property $G_m(y',y)=G_m(y,y')$, resulting in (39). In summary, the solution of the meridional circulation problem is

$$\psi(y,z,t)=e^{-z/2H}\sum_{m=0}^{\infty}\hat{\psi}_m(y,t)\mathcal{Z}_m(z), \tag{38}$$

where

$$\hat{\psi}_m(y,t)=-b_m\int_{-\infty}^{\infty}\frac{\partial F_m(y',t)}{\partial y'}G_m(y,y')dy'. \tag{39}$$

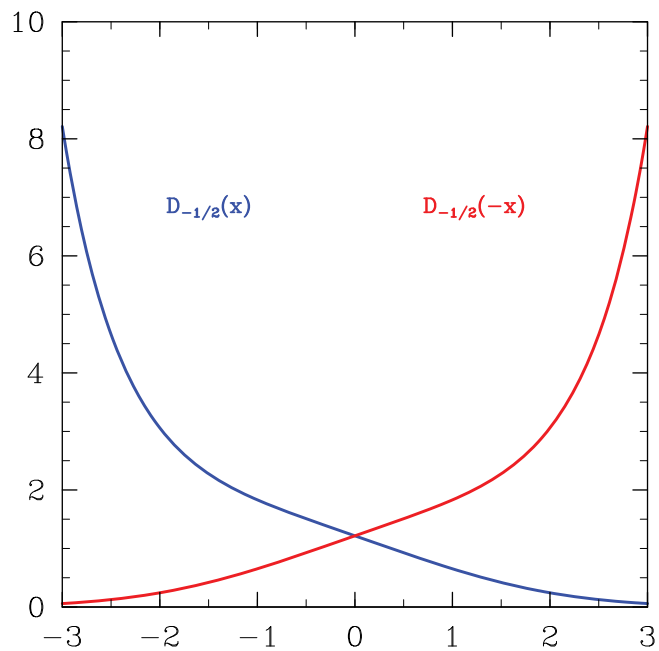

Figure 3. Parabolic cylinder functions $D_{-1/2}(x)$ and $D_{-1/2}(-x)$ for $-3 \le x \le 3$. The function $D_{-1/2}(x)$, shown by the blue curve, satisfies the $y \to \infty$ boundary condition and is used to construct the Green's function $G_m(y,y')$ north of y'. Similarly, the function $D_{-1/2}(-x)$, shown by the red curve, satisfies the $y \to -\infty$ boundary condition and is used to construct the Green's function $G_m(y,y')$ south of y'. Because these two parabolic cylinder functions are solutions of (33) with $\nu = -1/2$, their second derivatives are zero at the equator but become large away from the equator. All the calculations presented here use the Mathematica function ParabolicCylinderD[ν, x].

The solution for the stream function is obtained by first calculating $F_m(y',t)$ from (28), then calculating $\hat{\psi}_m(y,t)$ from (39), and finally calculating $\psi(y,z,t)$ from (38). Although this procedure generally involves the calculation of two integrals and an infinite sum, there are two special cases where the formulas (38 and 39) are considerably simplified. One corresponds to prescribed diabatic heating in the ITCZ, and the other corresponds to prescribed Ekman pumping at the top of the boundary layer. Making these prescribed fields step functions in y allows for analytical solutions. These idealized ITCZ forcings are introduced in the next two sections.

5. Deep Overturning Circulations

Now consider the response to a forcing that projects only onto the first internal mode and is constant in time. We begin by using (28),

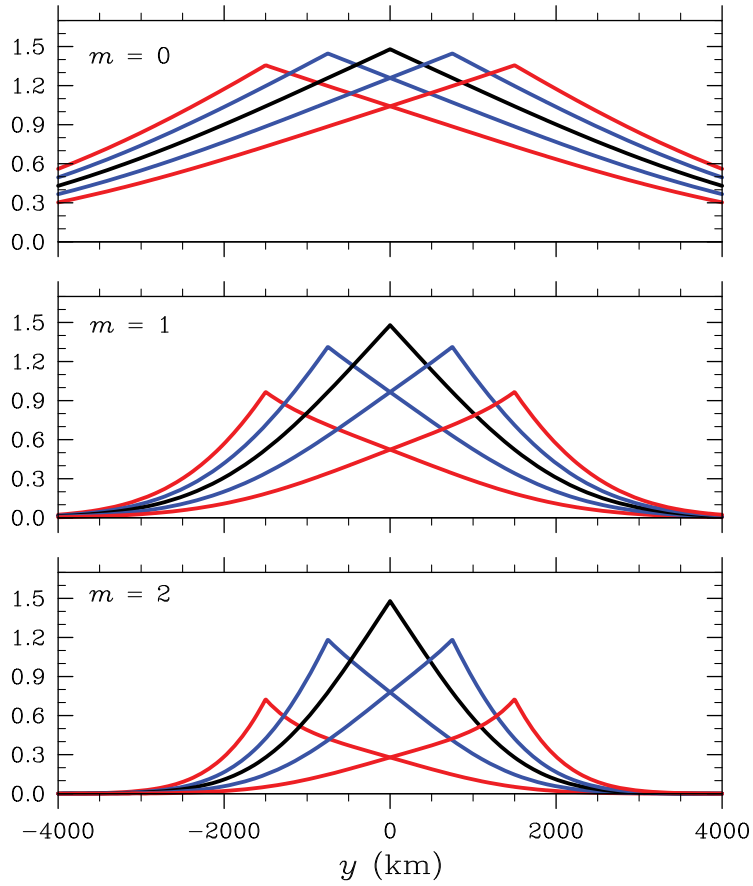

Figure 4. Green's functions $G_m(y, y')$ for $y' = -1500, -750, 0, 750, 1500$ km and for (top) $m = 0$, (middle) $m = 1$, and (bottom) $m = 2$. These curves have been computed from (36). Note that, because of the b_m factors in (36), the Green's functions become more confined as the vertical mode index m becomes larger.

along with the assumption of constant N, to write

$$F_m(y) = \frac{g\hat{Q}_m(y)}{c_p T_0 N^2} + \left(\mathcal{W}(y) - \frac{g\hat{Q}(y,0)}{c_p T_0 N^2}\right)\mathcal{Z}_m(0), \tag{40}$$

where

$$\hat{Q}_m(y) = \frac{N^2}{g}\int_0^{z_T} \hat{Q}(y,z)\mathcal{Z}_m(z)dz + \hat{Q}(y,0)\mathcal{Z}_m(0). \tag{41}$$

We assume that $\hat{Q}(y,z)$ vanishes everywhere except in the latitudinal range $y_1 < y < y_2$, where y_1 and y_2 are constants that specify the south and north boundaries of the ITCZ. Within the ITCZ, the diabatic heating is assumed to be independent of y and to have a vertical profile proportional to $\mathcal{Z}_1(z)$, i.e.,

$$\hat{Q}(y,z) = \begin{cases} \tilde{Q}\mathcal{Z}_1(z) & \text{if } y_1 < y < y_2, \\ 0 & \text{otherwise}, \end{cases} \tag{42}$$

where $\tilde{Q}$ will be given later. In addition, we assume that the vertical velocity at the top of the boundary layer is given by

$$\mathcal{W}(y) = \frac{g\hat{Q}(y,0)}{c_p T_0 N^2}. \tag{43}$$

Since we would like to use the vertical structure of only the first internal mode $\mathcal{Z}_1(z)$ as the vertical structure of the prescribed diabatic heating and the vertical structure of the first internal mode is nonzero at the top of the boundary layer (Figure 2), there has to be a nonzero $\mathcal{W}$ at $z = 0$.

Using these assumptions in (40) and (41), and then making use of the orthonormality relation (A2) we obtain

$$F_m(y)=\frac{g\tilde{Q}}{c_pT_0N^2}\begin{cases}1 & \text{if } m=1 \text{ and } y_1<y<y_2,\\ 0 & \text{otherwise}.\end{cases} \tag{44}$$

Many tropical regions have more complicated vertical diabatic heating profiles, such as the eastern Pacific, where heating profiles are more "bottom heavy" than the $\mathcal{Z}_1(z)$ profile, as illustrated in the studies of *Wu et al*. [2000], *Wang and Magnusdottir* [2005], *Zhang and Hagos* [2009], *Takayabu et al*. [2010], and *Ling and Zhang* [2013]. Due to this, the assumption that the diabatic heating is deep and made up of only the first internal mode is only meant to represent one aspect of heating in the tropical atmosphere, and it is the simplest case since it can be represented using only one vertical mode.

Use of (44) in (39) now yields

$$\begin{aligned}\hat{\psi}_1(y)&=-b_1\int_{-\infty}^{\infty}\frac{\partial F_1(y')}{\partial y'}G_1(y,y')dy'\\ &=-b_1G_1(y,y_1)\int_{y_1-}^{y_1+}\frac{\partial F_1(y')}{\partial y'}dy'-b_1G_1(y,y_2)\int_{y_2-}^{y_2+}\frac{\partial F_1(y')}{\partial y'}dy'\\ &=\frac{gb_1\tilde{Q}}{c_pT_0N^2}[G_1(y,y_2)-G_1(y,y_1)],\end{aligned} \tag{45}$$

where the final line in (45) follows from the fact that the narrow integral across $y=y_1$ is $[g\tilde{Q}/(c_pT_0N^2)]$, while the narrow integral across $y=y_2$ is $-[g\tilde{Q}/(c_pT_0N^2)]$. Use of (45) in (38), yields the final solution

$$\psi(y,z)=\frac{gb_1\tilde{Q}}{c_pT_0N^2}e^{-z/2H}\mathcal{Z}_1(z)[G_1(y,y_2)-G_1(y,y_1)], \tag{46}$$

where the Green's functions $G_1(y,y_1)$ and $G_1(y,y_2)$ are given in (36). Equation (46) is quite powerful. It states that only two Green's functions are needed in order to understand the meridional structure of the deep Hadley circulation. $G_1(y, y_2)$ gives the meridional structure of the stream function attributed to the jump in the diabatic heating at the north edge of the ITCZ, while $G_1(y, y_1)$ gives the meridional structure of the stream function attributed to the jump in the diabatic heating at the south edge of the ITCZ. All of the information about meridional asymmetries between the winter and summer deep Hadley cells is contained in these two Green's functions. The solution (46) can also be written in the form

$$\begin{aligned}\psi(y,z)&=\frac{gb_1\tilde{Q}}{c_pT_0N^2\sqrt{2}}e^{-z/2H}\mathcal{Z}_1(z)\\ &\times\begin{cases}[D_{-1/2}(y_2/b_1)-D_{-1/2}(y_1/b_1)]D_{-1/2}(-y/b_1) & \text{if } -\infty<y\le y_1,\\ D_{-1/2}(y_2/b_1)D_{-1/2}(-y/b_1)-D_{-1/2}(-y_1/b_1)D_{-1/2}(y/b_1) & \text{if } y_1\le y\le y_2,\\ [D_{-1/2}(-y_2/b_1)-D_{-1/2}(-y_1/b_1)]D_{-1/2}(y/b_1) & \text{if } y_2\le y<\infty.\end{cases}\end{aligned} \tag{47}$$

With these assumptions, the $(\partial\hat{Q}/\partial y)$-term on the right-hand side of (15) vanishes everywhere except along the edges of the ITCZ, where it becomes infinitely large over an infinitesimally thin layer. Thus, the circulation in the (y, z)-plane consists of a counterclockwise overturning cell on the southern edge of the ITCZ and a clockwise overturning cell in the northern edge of the ITCZ looking from east to west. Figure 5 shows these circulation cells via isolines of $\psi(y,z)$ computed from (47) using the parameters $z_T=13$ km, $N=1.2\times10^{-2}$ s^{-1}, $(y_1, y_2)=(0, 500)$, (500, 1000), (1000, 1500), (1500, 2000) km, and assuming that $\tilde{Q}=(c_p/B_1)$ 5 K d^{-1}, where B_1 is derived in Appendix B. The cross-equatorial cell, or winter cell, is significantly stronger than the summer cell, which is limited to the summer hemisphere. As the ITCZ is displaced further away from the equator, the meridional asymmetry between the winter and summer cell increases in Figures 5a–5c,

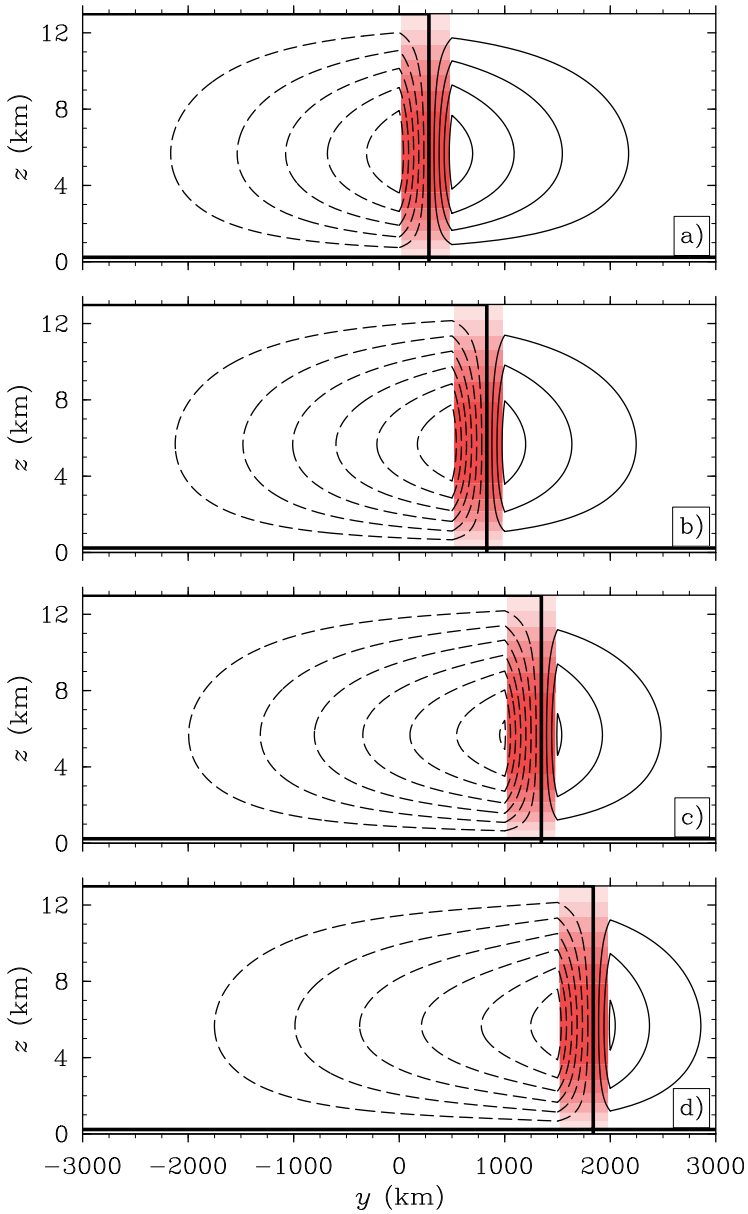

Figure 5. Contoured stream function $\psi(y, z)$ and shaded $Q(y,z)e^{-z/H}/c_p$ fields for four deep diabatic heating cases: (a) $(y_1, y_2) = (0, 500)$ km, (b) $(y_1, y_2) = (500, 1000)$ km, (c) $(y_1, y_2) = (1000, 1500)$ km, and (d) $(y_1, y_2) = (1500, 2000)$ km. The contour interval for $\psi(y,z)$ is 400 m^2 s^{-1}, the maximum (magnitude) of $\psi(y, z)$ is 2852 m^2 s^{-1}, and the zero line is of double thickness. The $Q(y,z)e^{-z/H}/c_p$ shade interval is 0.5 K d^{-1}, and the maximum (magnitude) of the diabatic heating is 3.496 K d^{-1}.

and decreases slightly in Figure 5d. The asymmetry between the two cells is attributed to the meridional asymmetry of the inertial stability parameter, $\beta^2 y^2$. The winter cell is located in a region where $\beta^2 y^2$ is either zero or close to zero, minimizing the turning due to the Coriolis force. When the ITCZ is far enough from the equator, the winter cell is mostly located off of the equator and can no longer efficiently extend into the low inertial stability near the equator. Therefore, the mass flux of the winter cell begins to decrease. These results are in general agreement with the numerical model results of *Hack et al.* [1989].

The meridional asymmetry between the two cells is also apparent in Figure 6, where 0–3 day parcel trajectories are computed from $v(y,z)$ and $w(y,z)$. The parcel trajectories agree well with *Schubert et al.* [1991]. The effects of inertial stability are also apparent in this figure since parcels on the northern edge of the ITCZ travel relatively high in the vertical direction and parcels on the southern edge of the ITCZ travel relatively

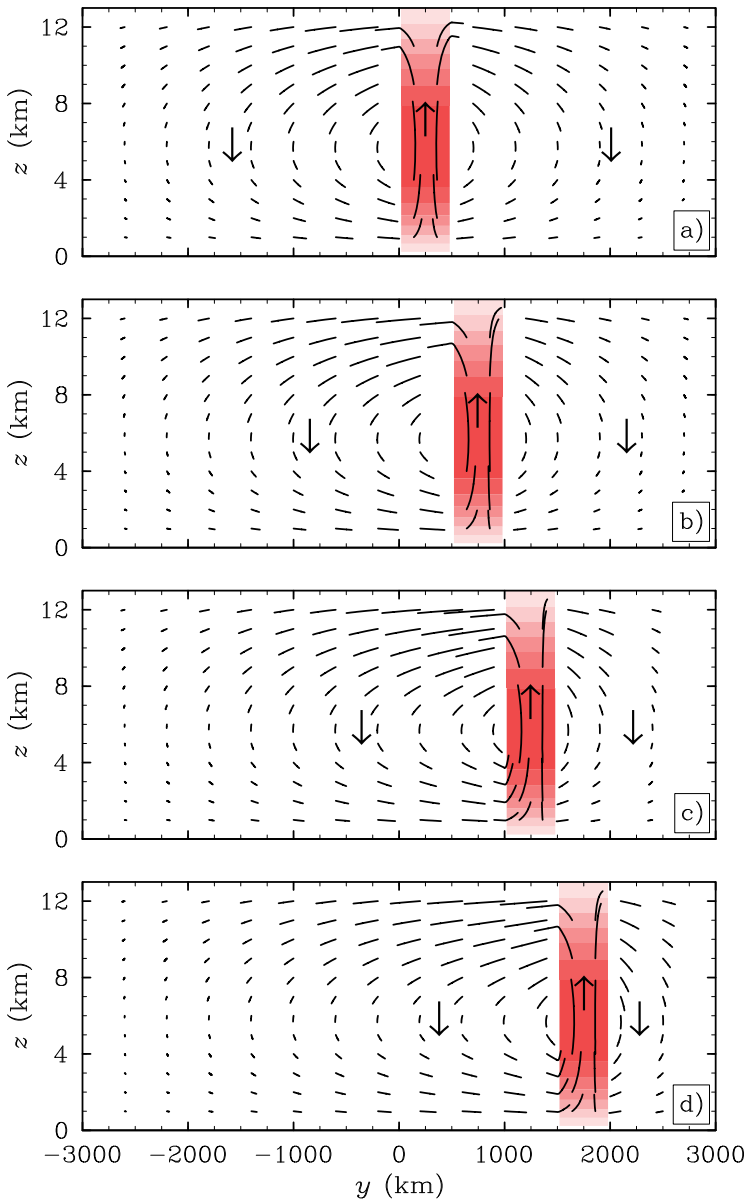

Figure 6. Parcel trajectories and shaded $Q(y,z)e^{-z/H}/c_p$ field (same as Figure 5) during the first 3 days for the four deep diabatic heating displacements mentioned in Figure 5. The arrows indicate the direction of the trajectories inside and outside of the ITCZ.

far in the meridional direction, even though the diabatic heating is constant in the ITCZ. Parcels in the southern part of the ITCZ feel lower inertial stability than parcels on the northern part of the ITCZ.

The approximate time scale it takes a parcel to complete one full cycle in either the winter or summer Hadley cell is 2–3 months. This time scale is at least an order of magnitude larger than the time it takes for the Hadley cells to equilibrate to the diabatic heating. Note that the zonal velocity is much larger than the meridional velocity, therefore by the time a parcel makes one meridional revolution it will be located at a different longitude, possibly having traveled an entire circle of latitude. Also, calculating such a time scale may be a bit more complicated since combined barotropic and baroclinic instability tends to occur as the zonal winds evolve.

Figure 7 shows contours of the $T_t(y, z)$ and $w(y,z)$ fields. It is not surprising that $w(y,z)$ is discontinuous in the meridional direction because the prescribed diabatic heating $\hat{Q}(y,z)$ is discontinuous in the meridional direction. Although, $T_t(y,z)$ is positive and smooth in the meridional direction, even across the edges of the ITCZ. T_t

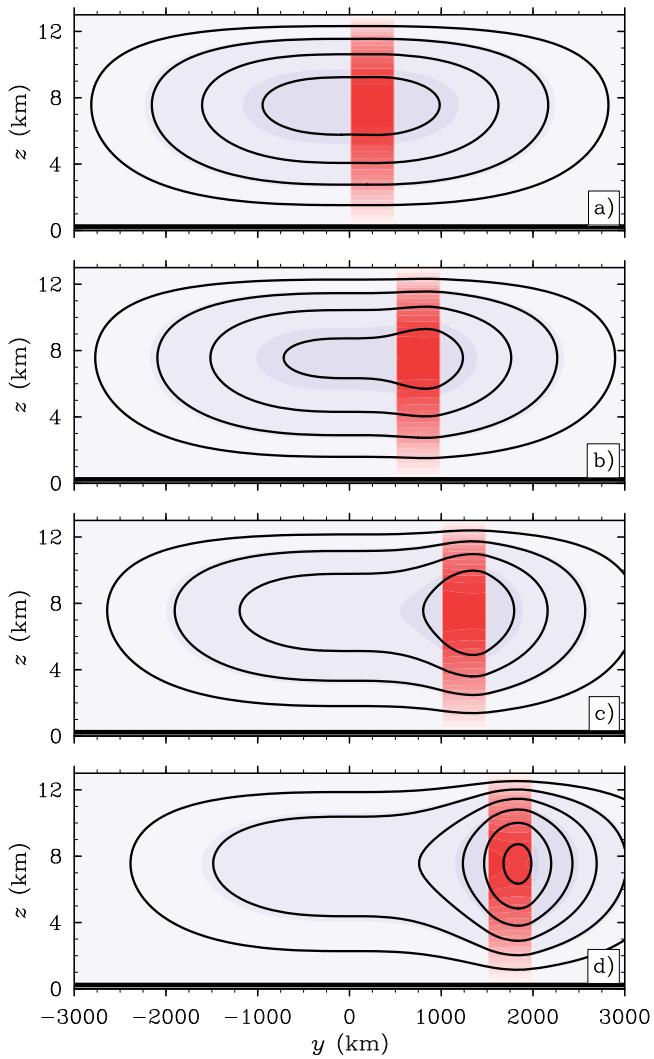

Figure 7. Contoured perturbation temperature tendency $T_t(y, z)$ and shaded log-pressure vertical velocity $w(y, z)$ for the four deep diabatic heating displacements mentioned in Figure 5. The $T_t(y, z)$ contour interval is 0.2 K d^{-1}, the maximum (magnitude) $T_t(y, z)$ is 1.257 K d^{-1}, and the zero line is of double thickness. The $w(y, z)$ shade interval is 1 mm s^{-1}, and the maximum (magnitude) $w(y, z)$ is 18.01 mm s^{-1}.

remains positive due to diabatic warming associated with concentrated rising motion in the ITCZ and adiabatic warming associated with broad subsidence outside of the ITCZ. The smooth nature of the temperature tendency field agrees with the idea that temperature gradients are small in the tropics. Also, notice the slight poleward displacement of the peak thermodynamic response in the ITCZ and the asymmetric changes in both $T_t(y,z)$ and $w(y,z)$ as the ITCZ is moved away from the equator.

Figure 8 shows contours of the $v(y, z)$ and $u_t(y, z)$ fields. The $v(y, z)$ field shows low-level convergence and upper-level divergence in and near the ITCZ. Also, the asymmetric response of $v(y, z)$ increases in Figures 8a–8c and decreases slightly in Figure 8d, similar to the $\psi(y, z)$ field. The low-level $u_t(y, z)$ field illustrates an increase of westerlies from the equator to slightly poleward of the center of the ITCZ and easterlies poleward of the westerlies. This meridional structure of the u_t implies a buildup of positive absolute vorticity in the ITCZ that satisfies the necessary condition for combined barotropic and baroclinic instability. At upper levels, the zonal velocity increases at a large rate, especially near the edges of the ITCZ. These upper-level zonal jets can be considered subtropical jets, but are different than jets seen in nature because zonally asymmetric eddies are neglected here.

Another view of combined barotropic and baroclinic instability comes from analyzing the potential vorticity anomaly. The potential vorticity equation is

$$\frac{\partial q}{\partial t}+\beta v=\frac{g\beta y}{c_p T_0 N^2}\left(\frac{\partial}{\partial z}-\frac{1}{H}\right)Q, \tag{48}$$

where

$$q=-\frac{\partial u}{\partial y}+\frac{g\beta y}{T_0 N^2}\left(\frac{\partial}{\partial z}-\frac{1}{H}\right)T \tag{49}$$

is the potential vorticity anomaly. A reversal of the meridional gradient of the total potential vorticity, $\beta y + q$, occurs on the poleward side of the ITCZ in the lower troposphere and on the equatorward side of the ITCZ in the upper troposphere in Figure 9, agreeing well with *Schubert et al.* [1991] and *Nieto Ferreira*

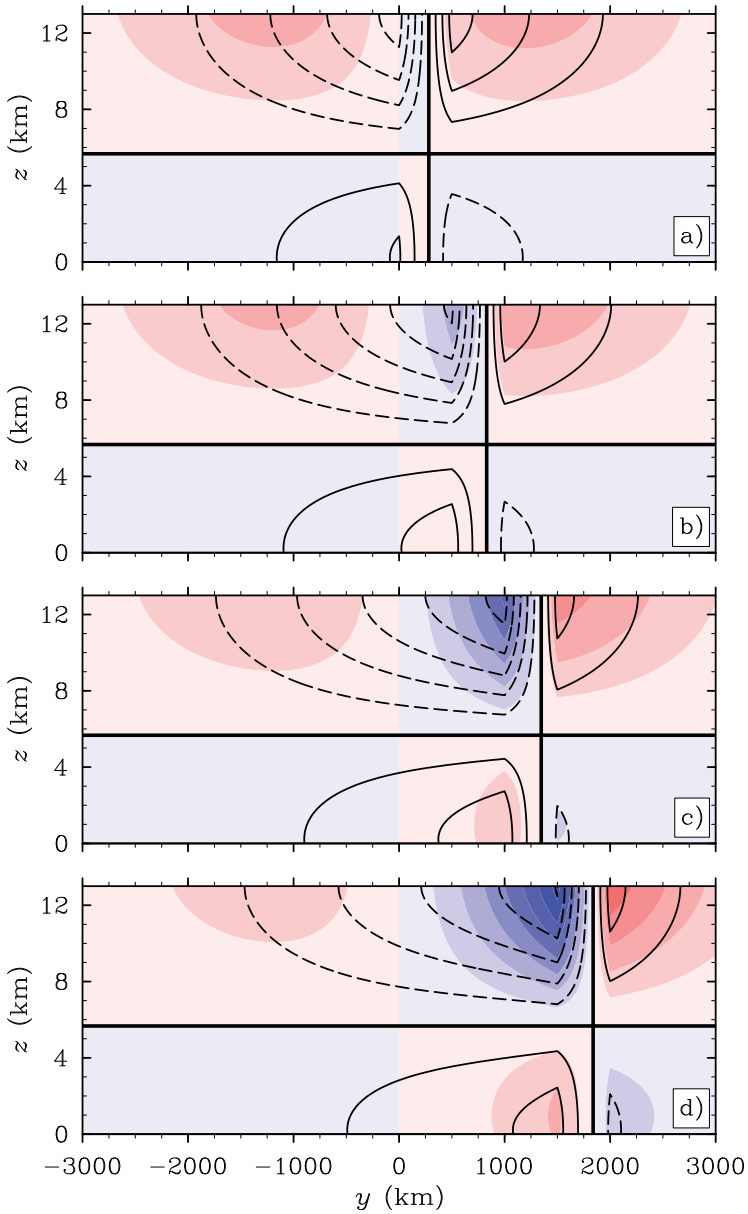

Figure 8. Contoured meridional velocity $v(y, z)$ and shaded zonal velocity tendency $u_t(y, z)$ for the four deep diabatic heating displacements mentioned in Figure 5. The $v(y, z)$ contour interval is 0.4 m s^{-1}, the maximum (magnitude) $v(y, z)$ is 2.141 m s^{-1}, and the zero line is of double thickness. The $u_t(y, z)$ shade interval is 1 m s^{-1} per day, and the maximum (magnitude) $u_t(y, z)$ is 7.403 m s^{-1} per day.

and Schubert [1997]. Thus, the necessary condition for combined barotropic-baroclinic instability is satisfied [*Charney and Stern*, 1962]. As the potential vorticity anomaly increases over time, growth rates of unstable waves are also expected to increase. In this sense, the ITCZ contains the seeds of its own destruction.

6. Shallow Overturning Circulations

While the direct effects of friction are confined to the boundary layer flow in the lowest kilometer, the inviscid interior is indirectly affected through the meridional circulation produced by the upward extension of the Ekman pumping at the top of the boundary layer, as discussed in *Holton et al.* [1971] and *Wang and Rui* [1990]. An estimate of the Ekman pumping at the top of the boundary layer in the ITCZ can be obtained by considering an idealized equatorial β-plane slab model linearized about a resting basic state of the region between 900 and 1013 hPa, a region which has the log-pressure depth $h_E = H \ln(1013/900) \approx 1015$ m. In this Ekman layer, the dynamics are governed by

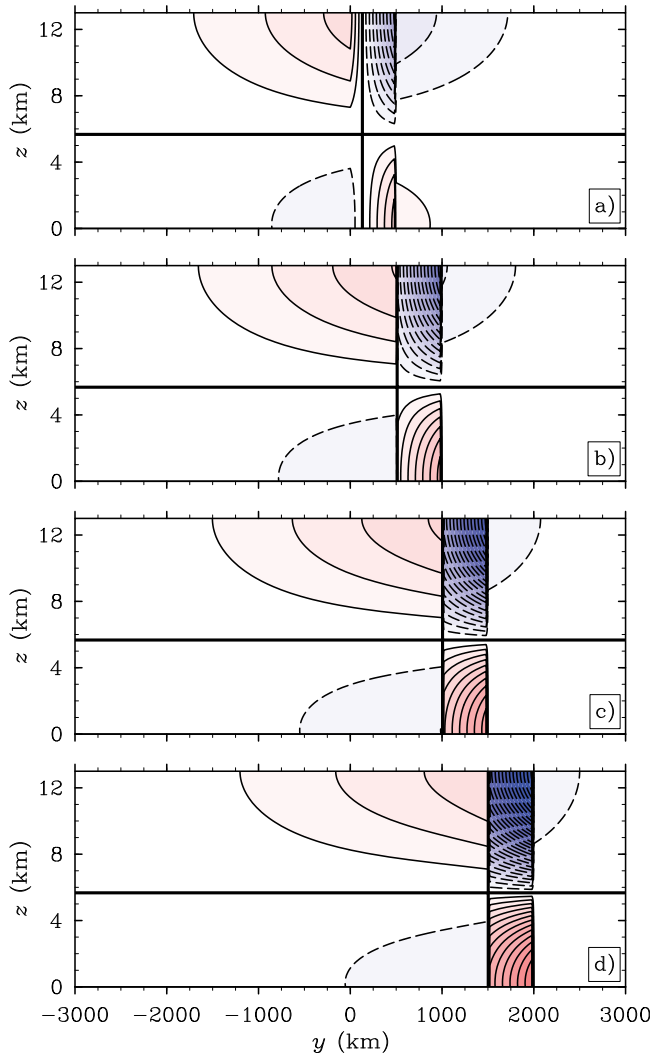

Figure 9. Potential vorticity anomaly tendency $q_t(y, z)$ for the four deep diabatic heating displacements mentioned in Figure 5. The $q_t(y, z)$ contour interval is 1×10^{-6} s^{-1} per day, the maximum (magnitude) is 2.927×10^{-5} s^{-1} per day, and the zero line is of double thickness.

$$\frac{\partial u_b}{\partial t} - \beta y v_b = -k u_b, \tag{50}$$

$$\frac{\partial v_b}{\partial t} + \beta y u_b = -k v_b + \beta y u_g, \tag{51}$$

$$-h_E \frac{\partial v_b}{\partial y} = w(y, 0, t) - w(y, -h_E, t) = \mathcal{W}(y, t), \tag{52}$$

where $u_b(y)$ and $v_b(y)$ are the height independent slab boundary layer velocity components, k is the proportionality constant for the surface stress, $\mathcal{W}$ is the Ekman pumping at the top of the boundary layer ($z = 0$), and $u_g(y)$ is the height independent geostrophic zonal velocity, which is defined in terms of the imposed pressure gradient force, $\partial\phi(y)/\partial y$, by

$$\beta y u_g = -\frac{\partial \phi}{\partial y}. \tag{53}$$

The first equality in equation (52) results from vertical integration of the Boussinesq form of the continuity equation (4). The second equality in equation (52) is obtained by first noting that $w(y, 0, t) = -(1/g)$

$[\partial\phi(y,0,t)/\partial t]+\mathcal{W}(y,t)$ and $w(y,-h_E,t)=-(1/g)[T_0/\bar{T}(-h_E)][\partial\phi(y,-h_E)/\partial t]$, since the physical height vertical velocity is assumed to vanish at $z=-h_E$. Also, note that $z<0$ is in the boundary layer and $z=0$ is the top of the boundary layer. The difference between these last two relations, with the assumption that $T_0/\bar{T}(-h_E)\approx 1$, yields the second equality in equation (52), since we assume the geopotential tendency is the same at all heights in the boundary layer.

For slowly evolving flows, the time derivative terms in (50) and (51) can be neglected, and then the resulting two algebraic equations can be solved to obtain

$$u_b(y)=\left(\frac{\beta^2y^2}{k^2+\beta^2y^2}\right)u_g(y), \tag{54}$$

$$v_b(y)=\left(\frac{k\beta y}{k^2+\beta^2y^2}\right)u_g(y). \tag{55}$$

As a typical example, $y_1=750$ km, $y_2=1250$ km, $u_g(y_1)=3.0$ m s^{-1}, $u_g(y_2)=-3.0$ m s^{-1}, and $k=8.3\times 10^{-6}$ s^{-1}, so that equations (54) and (55) yield

$$\begin{aligned} u_b(y_2)&=-2.78\text{ m s}^{-1}, \quad v_b(y_2)=-0.78\text{ m s}^{-1},\\ u_b(y_1)&=2.46\text{ m s}^{-1}, \quad v_b(y_1)=1.15\text{ m s}^{-1}. \end{aligned} \tag{56}$$

Using the values of $v_b(y_1)$ and $v_b(y_2)$ given in equations (56) and (52), we obtain the estimate

$$\mathcal{W}_{\text{ave}}\approx 1015\text{ m}\left(\frac{1.93\text{ m s}^{-1}}{500\text{ km}}\right)\approx 4\text{ mm s}^{-1} \tag{57}$$

for the average Ekman pumping in the ITCZ. Note that it is also possible to calculate a value of vertical velocity at the top of the boundary layer due to other processes. For example, the vertical velocity associated with boundary layer convergence due to SST gradients can be computed in a similar manner as done in *Stevens et al*. [2002] and *Back and Bretherton* [2009].

Based on the above estimate of Ekman pumping, and in order to isolate the effects of the upward penetration of Ekman pumping in (26), consider (28) for the case in which $\hat{Q}(y,z)=0$ and

$$\mathcal{W}(y)=\begin{cases}\mathcal{W}_{\text{ave}} & \text{if } y_1<y<y_2,\\ 0 & \text{otherwise}.\end{cases} \tag{58}$$

Use of (58) in (39) now yields

$$\begin{aligned} \hat{\psi}_m(y) &= -b_m\mathcal{Z}_m(0)\int_{-\infty}^{\infty}\frac{d\mathcal{W}(y')}{dy'}G_m(y,y')dy'\\ &= -b_m\mathcal{Z}_m(0)G_m(y,y_1)\int_{y_1-}^{y_1+}\frac{\partial\mathcal{W}(y')}{\partial y'}dy' - b_m\mathcal{Z}_m(0)G_m(y,y_2)\int_{y_2-}^{y_2+}\frac{\partial\mathcal{W}(y')}{\partial y'}dy'\\ &= b_m\mathcal{Z}_m(0)\mathcal{W}_{\text{ave}}\left[G_m(y,y_2)-G_m(y,y_1)\right], \end{aligned} \tag{59}$$

where the final line in (59) follows from the fact that the narrow integral across $y=y_1$ is $\mathcal{W}_{\text{ave}}$, while the narrow integral across $y=y_2$ is $-\mathcal{W}_{\text{ave}}$. Use of (59) in (19), along with (14), yields the final solution

$$\psi(y,z)=\mathcal{W}_{\text{ave}}e^{-z/2H}\sum_{m=0}^{\infty}b_m\mathcal{Z}_m(0)\mathcal{Z}_m(z)[G_m(y,y_2)-G_m(y,y_1)]. \tag{60}$$

This equation is a bit more complicated than the formula (46) for the deep Hadley circulation, but still quite insightful. Equation (60) states that a combination of Green's functions, Rossby lengths, and eigenfunctions

are needed in order to understand the meridional structure of the shallow Hadley circulation. The solution (60) can also be written in the form

$$\psi(y,z)=\mathcal{W}_{\text{ave}}\,e^{-z/2H}\sum_{m=0}^{\infty}b_m\mathcal{Z}_m(0)\mathcal{Z}_m(z)$$
$$\times\begin{cases}[D_{-1/2}(y_2/b_m)-D_{-1/2}(y_1/b_m)]D_{-1/2}(-y/b_m) & \text{if } -\infty<y\le y_1,\\ D_{-1/2}(y_2/b_m)D_{-1/2}(-y/b_m)-D_{-1/2}(-y_1/b_m)D_{-1/2}(y/b_m) & \text{if } y_1\le y\le y_2,\\ [D_{-1/2}(-y_2/b_m)-D_{-1/2}(-y_1/b_m)]D_{-1/2}(y/b_m) & \text{if } y_2\le y<\infty.\end{cases} \tag{61}$$

Using the prescribed Ekman pumping at the top of the boundary layer, the $(\partial\mathcal{W}/\partial y)$-term on the right-hand side of (18) vanishes everywhere except along the edges of the ITCZ, analogous to the deep diabatic heating case. Taking the assumed Ekman convergence in the boundary layer into consideration, the circulation in the (y, z)-plane consists of a counterclockwise overturning cell on the southern edge of the ITCZ and a clockwise overturning cell on the northern edge of the ITCZ looking from east to west. Figure 10 shows the top half of the circulation cells via isolines of $\psi(y,z)$ computed from (56) using the same parameters as for the deep diabatic heating case, $\mathcal{W}_{\text{ave}}=4$ mm s^{-1}, and $(y_1,y_2)=(0,500),(500,1000),(1000,1500),(1500,2000)$ km. The solutions have been computed using a maximum vertical wave number of $m=500$, and only the region up to $z=3$ km is displayed since the solution is negligible above $z=3$ km. The meridional overturning circulation is strongly trapped just above the boundary layer because the resistance of parcels to horizontal motion (i.e., inertial stability) is significantly smaller than their resistance to vertical motion (i.e., static stability). The mass flux of the winter cell is significantly stronger than that of the summer cell, just like the deep Hadley circulation. As the ITCZ is displaced further away from the equator, the meridional asymmetry between the winter and summer cells increases for all of the displacements due once again to the anisotropy of the inertial stability.

In order to see the asymmetric nature of the shallow Hadley circulation in more detail, 0–3 day parcel trajectories calculated from $v(y, z)$ and $w(y, z)$ are illustrated in Figure 11 for the three off-equatorial ITCZ positions: $(y_1,y_2)=(500,1000),(1000,1500),(1500,2000)$ km. For cases in which the ITCZ touches or straddles the equator (not shown), the numerical convergence of the $v(y,z)$ and $w(y,z)$ fields is slow because the shallow return circulation is so strongly trapped just above the top of the boundary layer. The approximate time scale it takes a parcel near the top of the boundary layer in the ITCZ to cross the equator depends greatly on the displacement of the ITCZ, but is on the order of 7 days in (a) to 2 months in (c).

Figure 12 illustrates contours of $v(y, z)$ for the ITCZ positions: $(y_1,y_2)=(500,1000),(1000,1500),(1500,2000)$ km. There is meridional divergence at the top of the boundary layer with maximum meridional winds of 3–7 m s^{-1}, which generally agree with *Zhang et al.* [2004]. Despite these relatively large values of $v(y, z)$, the response of $v(y, z)$ to the Ekman pumping is relatively weak in the southern hemisphere compared to the deep Hadley circulation, except for Figure 12a.

The cross-equatorial meridional winds at the top of the boundary layer may have implications for moisture transport across the equator, as mentioned in both *Zhang et al.* [2004] and *Nolan et al.* [2007]. As the ITCZ migrates closer to the equator during December to February in the eastern Pacific, the cross-equatorial winds at the top of the boundary layer increase in the winter cell of the shallow Hadley circulation. These cross-equatorial winds advect moisture across the equator, and along with warmer SSTs south of the equator, may help in setting up favorable conditions for an ITCZ south of the equator. Therefore, a double ITCZ is more likely to been seen during the months after the ITCZ is close but strictly north of the equator. As the ITCZ north of the equator begins to migrate poleward again, the cross-equatorial winds at the top of the boundary layer and SSTs south of the equator decrease, leading to less favorable conditions for an ITCZ south of the equator.

In Figure 13, the vertical log-pressure velocity $w(y, z)$ is contoured for the three ITCZ positions: $(y_1,y_2)=(500,1000),(1000,1500),(1500,2000)$ km. There is rising motion in and near the ITCZ up to $z\approx 2$ km, and weak sinking motion away from the ITCZ. As the ITCZ is displaced farther away from the equator, parcels are pumped to higher levels due to the increase in inertial stability going toward the pole. Also, note that the $T_t(y, z)$ field has the same structure as $w(y, z)$, but with opposite signs (not shown). There

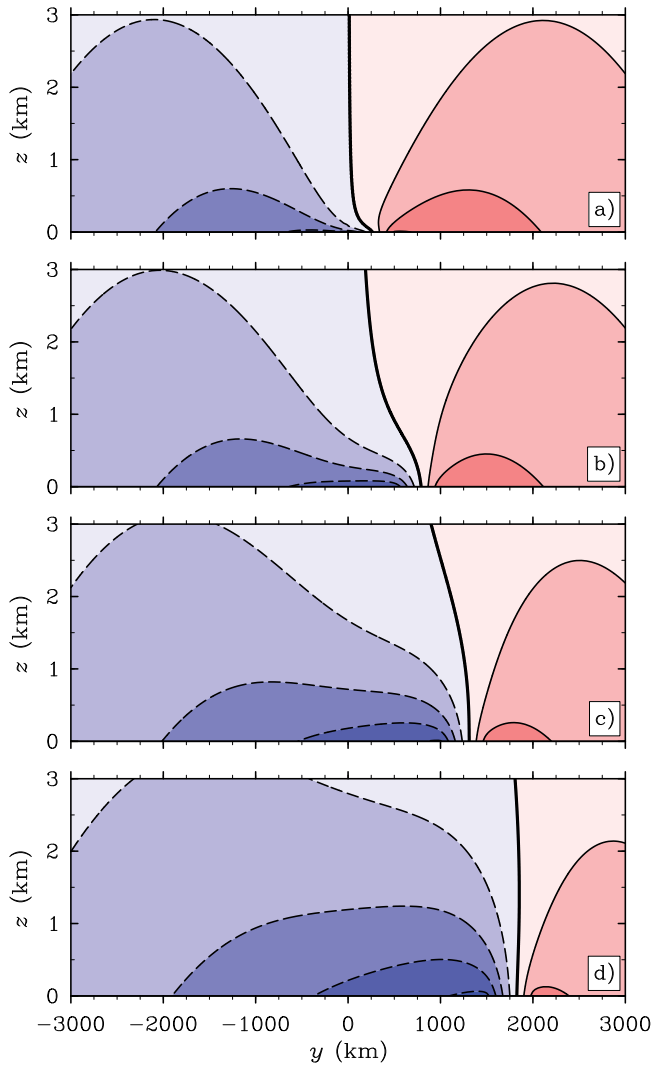

Figure 10. Contoured stream function $\psi(y, z)$ for the four displacements mentioned in Figure 5. The contour interval is 400 $m^2 s^{-1}$, the maximum (magnitude) $\psi(y, z)$ is 1723 $m^2 s^{-1}$, and the zero line is of double thickness. Note: the domain is $0 \leq z \leq 3$, where $z = 0$ is the top of the boundary layer.

is adiabatic cooling where $w(y, z) > 0$ and adiabatic warming where $w(y, z) < 0$, with a maximum perturbation temperature tendency at the top of the ITCZ boundary layer. This result agrees with the theory from *Nolan et al*. [2007] that shallow overturning circulations are associated with a reversal of the temperature gradient between the ITCZ and away from the ITCZ at the top of the boundary layer.

Observations [*Zhang et al*., 2004] and numerical modeling studies [*Nolan et al*., 2007, 2010] tend to show that there are distinct multilevel flows in the ITCZ associated with deep and shallow circulations. Therefore, we decided to show the $\psi(y, z)$ solution when both forcings are present (Figure 14). Both the deep and shallow Hadley circulations are present, especially when the ITCZ is close to equator. Taking the assumed boundary layer convergence into consideration, the divergence just above the top of the boundary layer along with convergence until about the middle troposphere and divergence at upper levels is in general agreement with the studies mentioned above.

7. Asymmetrical Nature of the Hadley Circulation

The meridional asymmetry of the winter and summer cells in both Hadley circulations so far has only been discussed when the ITCZ is 500 km wide. A compact formula can be derived of the fractional asymmetry

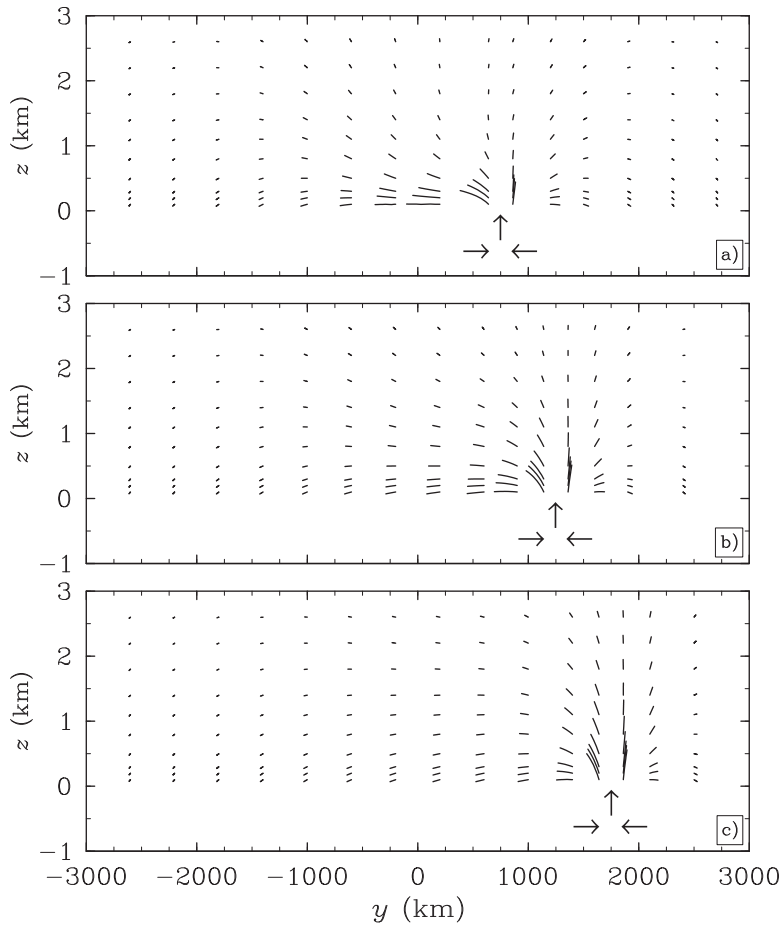

Figure 11. Parcel trajectories during the first 3 days for three Ekman pumping displacements: (a) $(y_1, y_2) = (500, 1000)$ km, (b) $(y_1, y_2) = (1000, 1500)$ km, and (c) $(y_1, y_2) = (1500, 2000)$ km. Note: the domain is $-1 \le z \le 3$, where $z = 0$ is the top of the boundary layer. The arrows indicate the direction of the boundary layer inflow and associated Ekman pumping.

between the two cells for ITCZs of any width. The maximum mass flux of the winter cell occurs at $y = y_1$ and the maximum mass flux of the summer cell occurs at $y = y_2$ when the ITCZ is north of the equator. Therefore, the fractional mass flux in the summer Hadley cell as a function of vertical wave number m is

$$\frac{\hat{\psi}_m(y_2)}{\hat{\psi}_m(y_2)-\hat{\psi}_m(y_1)} = \left\{1-\frac{D_{-1/2}(y_2/b_m)}{D_{-1/2}(-y_1/b_m)}\left[\frac{D_{-1/2}(-y_2/b_m)-D_{-1/2}(-y_1/b_m)}{D_{-1/2}(y_2/b_m)-D_{-1/2}(y_1/b_m)}\right]\right\}^{-1}, \tag{62}$$

and the fractional mass flux in the winter Hadley cell as a function of vertical wave number m is

$$\frac{-\hat{\psi}_m(y_1)}{\psi_m(y_2)-\hat{\psi}_m(y_1)} = \left\{1-\frac{D_{-1/2}(-y_1/b_m)}{D_{-1/2}(y_2/b_m)}\left[\frac{D_{-1/2}(y_2/b_m)-D_{-1/2}(y_1/b_m)}{D_{-1/2}(-y_2/b_m)-D_{-1/2}(-y_1/b_m)}\right]\right\}^{-1}. \tag{63}$$

Now consider the limiting case where $(y_2-y_1) \to 0$, but $\tilde{Q} \to \infty$ in such a way that $\tilde{Q}(y_2-y_1)=$constant. Equation (47) reduces to

$$\psi(y,z) = \frac{g\tilde{Q}(y_2-y_1)}{c_p T_0 N^2\sqrt{2}} e^{-z/2H}\mathcal{Z}_1(z)\begin{cases} D'_{-1/2}(y_1/b_1)D_{-1/2}(-y/b_1) & \text{if } -\infty < y < y_1 \\ D'_{-1/2}(-y_1/b_1)D_{-1/2}(y/b_1) & \text{if } y_1 < y < \infty, \end{cases} \tag{64}$$

where $D'_{-1/2}(x)=dD_{-1/2}(x)/dx$ and $D'_{-1/2}(-x)=dD_{-1/2}(-x)/dx$. Note that $\psi(y,z)$ is discontinuous at $y = y_1$. With the aid of (35), the fractional mass flux in the summer hemisphere cell as a function of vertical wave number m for an infinitesimally thin ITCZ is

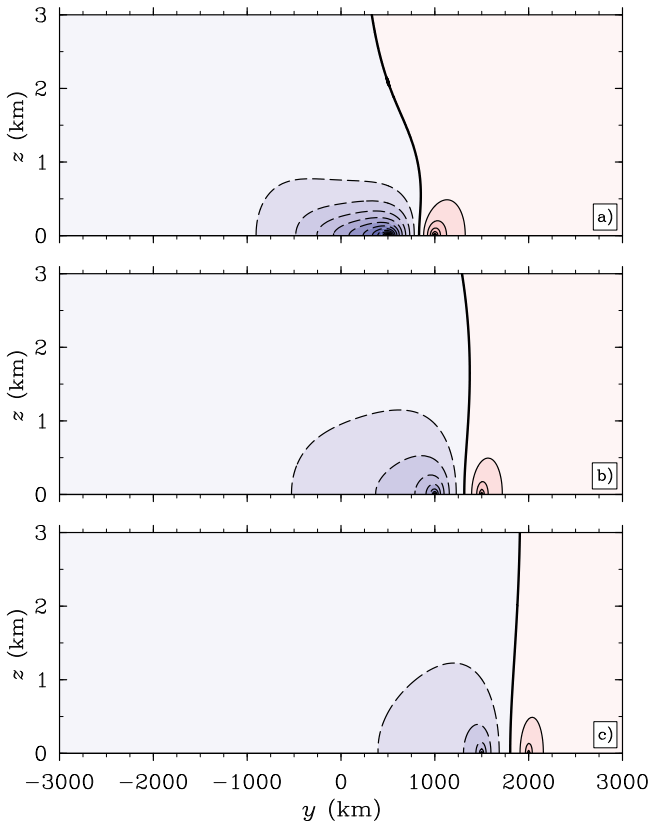

Figure 12. Contoured meridional velocity $v(y,z)$ for the three Ekman pumping displacements mentioned in Figure 11. The $v(y, z)$ contour interval is 0.4 m s^{-1}, the maximum (magnitude) $v(y,z)$ is 7.922 m s^{-1}, and the zero line is of double thickness. Note: the domain is $0 \le z \le 3$, where $z = 0$ is the top of the boundary layer.

$$(\text{Summer Cell})_m = \frac{\hat{\psi}_m(y_1^+)}{\hat{\psi}_m(y_1^+)-\hat{\psi}_m(y_1^-)} = \frac{1}{\sqrt{2}} D'_{-1/2}(-y_1/b_m) D_{-1/2}(y_1/b_m), \tag{65}$$

and the fractional mass flux in the winter hemisphere cell as a function of vertical wave number m for an infinitesimally thin ITCZ is

$$(\text{Winter Cell})_m = \frac{-\hat{\psi}_m(y_1^-)}{\hat{\psi}_m(y_1^+)-\hat{\psi}_m(y_1^-)} = -\frac{1}{\sqrt{2}} D'_{-1/2}(y_1/b_m) D_{-1/2}(-y_1/b_m). \tag{66}$$

Plots of (62), (63), (65), and (66) are shown in Figure 15 for $m = 0, 1, 2$ and for the four ITCZ widths: $(y_2-y_1) \to 0, (y_2-y_1)=500, 1000, 2000$ km. For example, when $m = 1$, the winter cell carries approximately 2–4 times the mass flux of the summer cell, increasing as the width of the ITCZ increases. This result is in close agreement with the numerical calculations of *Hack et al.* [1989] and *Hack and Schubert* [1990]. As m increases, the asymmetry between the winter and summer cells also increases. Complicated heating structures force higher vertical modes, therefore we expect there to be larger asymmetries between the winter and summer cells compared to the typical $m = 1$ mode. Both the width and vertical structure of diabatic heating in the ITCZ help explain the large observed asymmetries between the zonally and monthly averaged Hadley cells.

Now consider the fractional mass flux for Ekman pumping in the ITCZ in the absence of diabatic heating. The fractional mass flux in the shallow summer Hadley cell for an infinitesimally thin ITCZ is

$$\text{Summer Cell} = \frac{\psi(y_1^+, z)}{\psi(y_1^+, z)-\psi(y_1^-, z)} = \frac{\sum_{m=0}^{\infty} b_m \mathcal{Z}_m(0) \mathcal{Z}_m(z) D'_{-1/2}(-y_1/b_m) D_{-1/2}(y_1/b_m)}{\sum_{m=0}^{\infty} b_m \mathcal{Z}_m(0) \mathcal{Z}_m(z)}, \tag{67}$$

and the fractional mass flux in the shallow winter Hadley cell for an infinitesimally thin ITCZ is

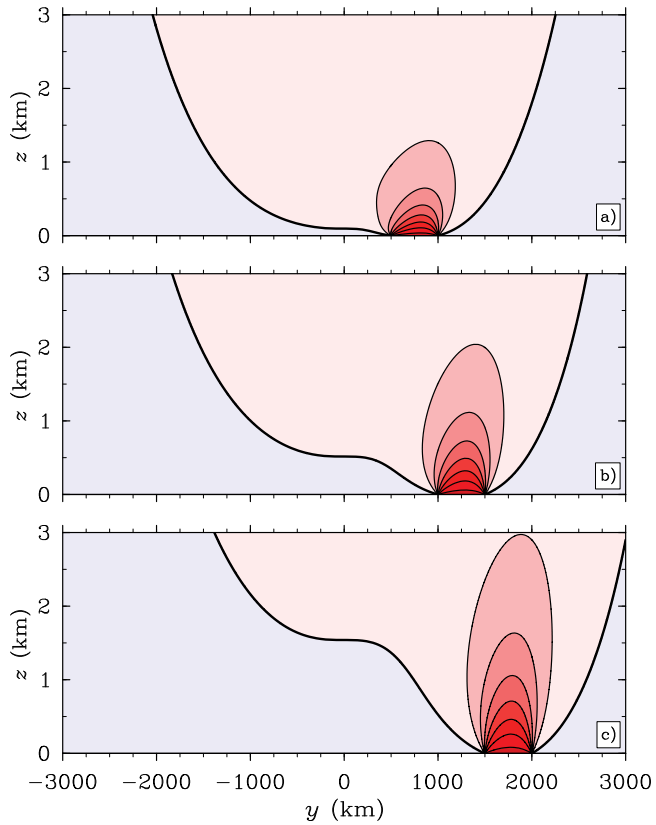

Figure 13. Contoured vertical log-pressure velocity $w(y,z)$ for the three Ekman pumping displacements mentioned in Figure 11. The $w(y,z)$ contour interval is 0.5 mm s^{-1}, the maximum (magnitude) $w(y,z)$ is 3.774 mm s^{-1}, and the zero line is of double thickness. Note: there is a discontinuity in $\mathcal{W}(z{=}0)$ at $y = y_1$ and $y = y_2$, and the domain is $0 \le z \le 3$, where $z = 0$ is the top of the boundary layer.

$$\text{Winter Cell} \quad = \frac{-\psi(y_1^-,z)}{\psi(y_1^+,z)-\psi(y_1^-,z)} \quad = -\frac{\sum_{m=0}^{\infty} b_m \mathcal{Z}_m(0)\mathcal{Z}_m(z) D'_{-1/2}(y_1/b_m) D_{-1/2}(-y_1/b_m)}{\sum_{m=0}^{\infty} b_m \mathcal{Z}_m(0)\mathcal{Z}_m(z)}. \tag{68}$$

Plots of (67) and (68) at $z = 0$ are shown in Figure 16. The maximum asymmetry between the winter and summer shallow Hadley cells occurs relatively far from the equator (2800–2900 km). This result is surprising since the shallow Hadley circulation was expected to be made up of many high vertical wave numbers, which decrease in equatorial Rossby length as m increases. Below the total solution in Figure 15, the contributions by the $m = 0, 1, 2$ modes are illustrated, and they show that the majority of the solution is comprised of the external $m = 0$ mode solution (more than 95% of the total solution). The external mode tends to play a large role in solutions at the lower boundary, as discussed in *Fulton* [1980]. It is also interesting to note that as z increases, the contributions from higher m modes increases, therefore the maximum asymmetry between the winter and summer cells changes in magnitude and location as a function of z. The location of maximum asymmetry between the winter and summer cells seems to depend highly on the dominant vertical normal modes in the ITCZ so that as vertical wave number increases, the solutions become more confined in the meridional direction (refer to the Green's function). The change in asymmetry between the winter and summer shallow Hadley cells as the ITCZ widens is not shown since the results are consistent with the results for the diabatic heating. In fact, the ideas of asymmetry are quite similar for both the deep and shallow Hadley circulations. The main difference lies in their spectrum of equatorial Rossby lengths.

8. Concluding Remarks

In this study, the effects of diabatic heating and Ekman pumping in the ITCZ were explored using an idealized model on the equatorial β-plane. The analysis used a linear zonally symmetric model of the inviscid

interior of the tropical atmosphere forced by two prescribed forcings in the ITCZ: (i) deep diabatic heating and (ii) Ekman pumping at the top of the boundary layer. The results demonstrate that deep diabatic heating in the ITCZ forces a deep overturning circulation in the absence of Ekman pumping, which we call the deep Hadley circulation. When Ekman pumping at the top of the boundary layer is present, there is a shallow overturning circulation, with divergence at the top of the boundary layer up to about 2 km above the top of the boundary layer, which we refer to as the shallow Hadley circulation. Both forcings illustrate an increase in asymmetry between the winter and summer Hadley cells until the ITCZ is displaced at a particular distance away from the equator. This distance depends on the dominant vertical normal modes in the ITCZ so that as vertical wave number increases, the solutions become more confined in the meridional direction.

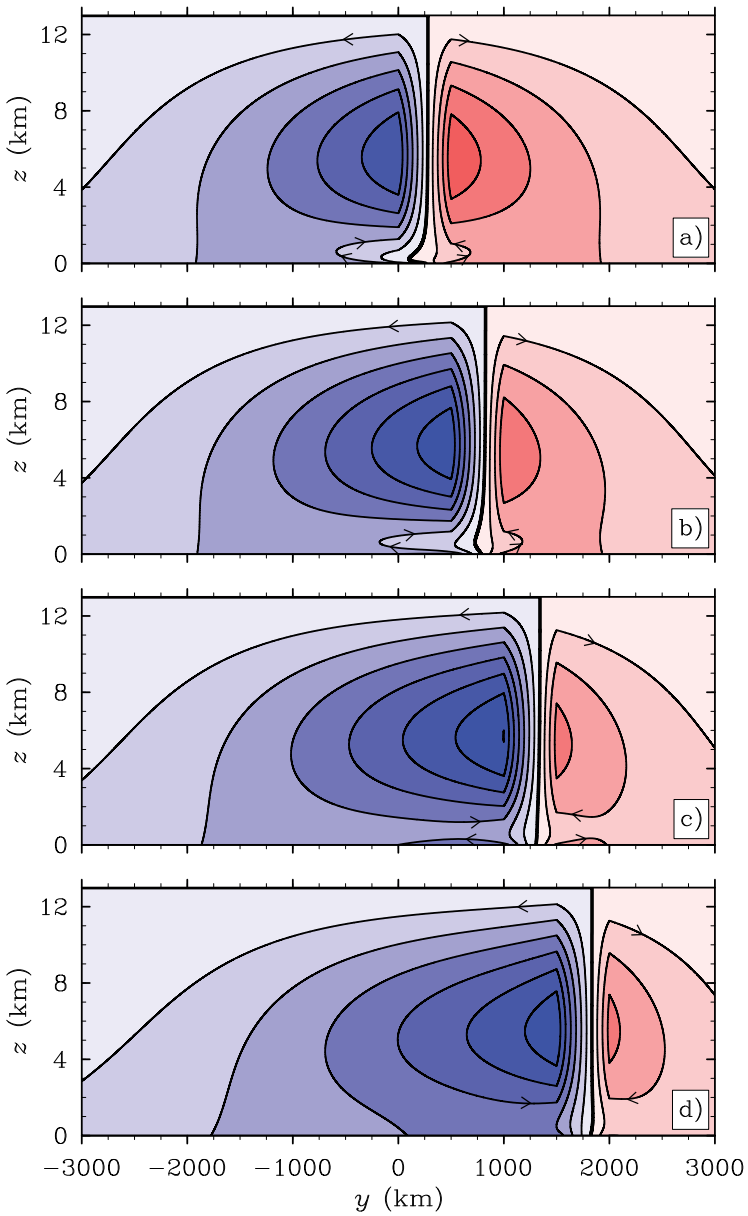

Figure 14. Contoured stream function $\psi(y,z)$ of both Ekman pumping and deep diabatic heating for the four displacements mentioned in Figure 5. The contour interval of $\psi(y,z)$ is 400 $m^2\ s^{-1}$, the maximum (magnitude) $\psi(y,z)$ is 2808 $m^2\ s^{-1}$, and the zero line is of double thickness. The arrow heads indicate the general direction of the flow field.

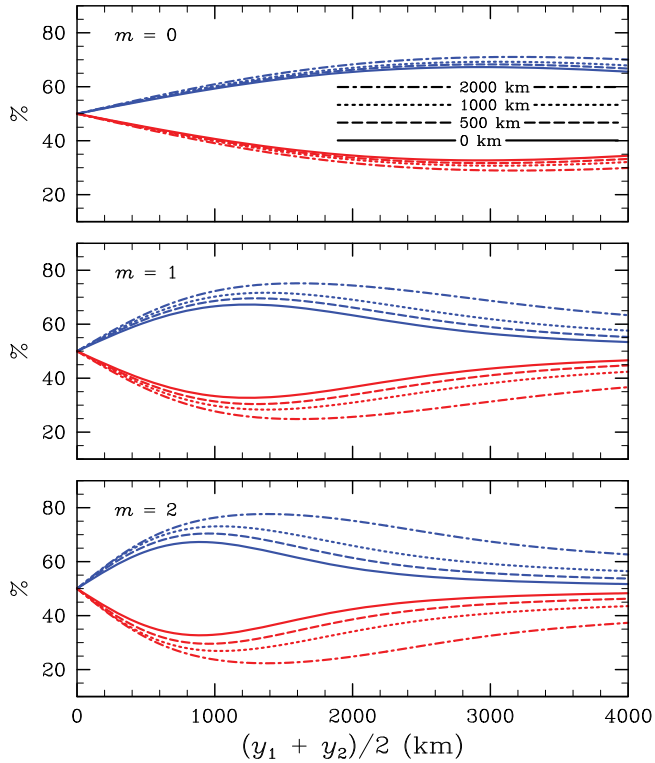

Figure 15. Percentage of the total mass flux carried by the summer hemisphere Hadley cell (red curves) and the winter hemisphere Hadley cell (blue curves) forced by diabatic heating for four ITCZ widths: infinitesimally thin $(y_2 - y_1) \to 0$, $(y_2 - y_1) = 500, 1000, 2000$ km. Three vertical modes are shown, $m = 0, 1, 2$.

The solution method described in section 3 begins with a vertical transform that involves solving the Sturm-Liouville problem, with a nonzero lower boundary condition, and then solves the horizontal structure equation (26) using Green's function since it obeys an equation similar to the ψ field. The fields that force the response in the ITCZ using the idealized equatorial β-plane model are the meridional structure of the diabatic heating and the Ekman pumping at the top of the boundary layer, while the inertial stability and static stability are shaping parameters. Since the static stability is constant in the solutions presented here, the spatial variability of the inertial stability $\beta^2 y^2$ plays the most important role in the asymmetry between the winter and summer Hadley cells. A physical interpretation is that fluid parcels forced near the equator by diabatic and frictional processes tend to move much more easily in the horizontal direction because the resistance to horizontal motion (i.e., inertial stability) is significantly smaller than the resistance to vertical motion (i.e., static stability). The asymmetries inherent in both the deep and shallow Hadley circulations were also explored for different ITCZ widths. The results indicate that as the ITCZ becomes wider, the asymmetry increases, agreeing well with *Hack and Schubert* [1990]. A new finding is that as the vertical structure of the forcing becomes more complicated (as vertical wave number increases), the asymmetry increases as well. The asymmetries between the winter and summer shallow Hadley cells at $z = 0$ that this model produces have somewhat of a different structure than expected since the majority of the solution is comprised of the external $m = 0$ vertical mode solution. In a model where the boundary layer is explicitly simulated, the shallow Hadley solution may look slightly different because it may have a larger percentage of contributions from higher internal vertical modes.

Future research on the topic of deep and shallow overturning circulations should explore a model that is able to produce solutions of both the boundary layer and the inviscid interior and should explore the role of higher internal modes. Such a model should also explore the role of combined barotropic and baroclinic instability as well as the effect of the basic state fields on the shallow Hadley circulation. The idealized model used in this study suffers from not being able to explore such aspects. The understanding of the ITCZ in the eastern Pacific involves ITCZ breakdown and diabatic heating dominates the monthly average solution, leading to deep overturning circulations. The time period between ITCZ breakdown and reformation is influenced by boundary layer processes, and most likely, shallow overturning circulations. It is still unclear whether shallow overturning circulations are due mostly to shallow diabatic heating or boundary layer effects such as Ekman pumping or vertical motion due to SST gradients. Therefore, the prevalence of shallow precipitating profiles and their contribution to shallow overturning circulations should also be explored.

Appendix A: Vertical Transform

The mathematical principles underlying the vertical transform pair (19) and (20) are the orthonormality and completeness of the eigenfunctions $\mathcal{Z}_m(z)$. Consider the eigenfunction $\mathcal{Z}_m(z)$, which is a solution of (21–23), and the eigenfunction $\mathcal{Z}_{m'}(z)$, which is a solution of (21–23) with m replaced by m'. To obtain the orthonormality relation, we multiply the equation for $\mathcal{Z}_m(z)$ by $\mathcal{Z}_{m'}(z)$, then multiply the equation for $\mathcal{Z}_{m'}(z)$ by $\mathcal{Z}_m(z)$, and finally integrate the difference of the resulting equations to obtain

$$\frac{1}{g}\left(\frac{1}{h_m}-\frac{1}{h_{m'}}\right)\int_0^{z_T}\mathcal{Z}_m(z)\mathcal{Z}_{m'}(z)N^2(z)dz+\left[\mathcal{Z}_{m'}(z)\frac{d\mathcal{Z}_m(z)}{dz}-\mathcal{Z}_m(z)\frac{d\mathcal{Z}_{m'}(z)}{dz}\right]_0^{z_T}=0. \tag{A1}$$

The second line in (A1) can be evaluated with the aid of the boundary conditions (22) and (23). Then, for distinct eigenvalues ($h_m \neq h_{m'}$) and for normalized $\mathcal{Z}_m(z)$, there is an orthonormality relation

$$\frac{1}{g}\int_0^{z_T}\mathcal{Z}_m(z)\mathcal{Z}_{m'}(z)\ N^2(z)dz+\mathcal{Z}_m(0)\mathcal{Z}_{m'}(0)=\begin{cases}1 & \text{if } m=m'\\ 0 & \text{if } m\neq m'.\end{cases} \tag{A2}$$

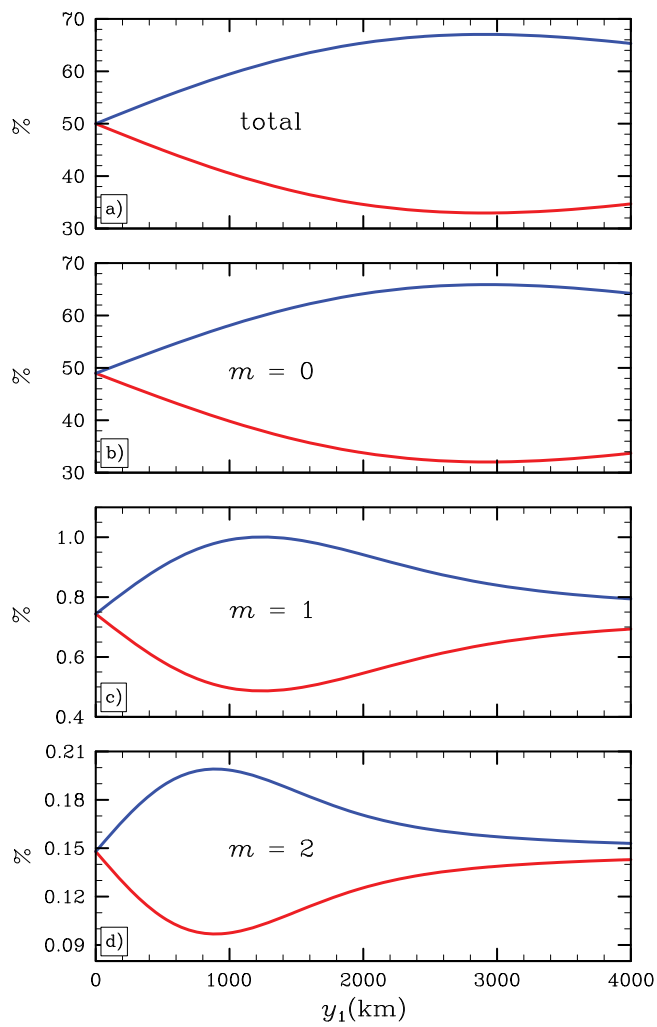

Figure 16. Percentage of the total mass flux carried by the summer hemisphere Hadley cell (red curves) and the winter hemisphere Hadley cell (blue curves) forced by Ekman pumping at the top of the boundary layer for an infinitesimally thin ITCZ. The four plots signify: (a) total solution, (b) contribution from the $m = 0$ mode, (c) contribution from the $m = 1$ mode, and (d) contribution from the $m = 2$ mode.

To confirm that (19) is the proper transform for the expansion (20), we multiply (20) by $\mathcal{Z}_{m'}(z)N^2(z)$ and then integrate over z to obtain

$$\int_0^{z_T}\hat{\psi}(y,z)\mathcal{Z}_{m'}(z)N^2(z)dz =\sum_{m=0}^{\infty}\hat{\psi}_m(y)\int_0^{z_T}\mathcal{Z}_m(z)\mathcal{Z}_{m'}(z)N^2(z)dz. \tag{A3}$$

Similarly, we multiply (20), evaluated at $z = 0$, by $\mathcal{Z}_{m'}(0)$ to obtain

$$\hat{\psi}(y,0)\mathcal{Z}_{m'}(0)=\sum_{m=0}^{\infty}\hat{\psi}_m(y)\mathcal{Z}_m(0)\mathcal{Z}_{m'}(0). \tag{A4}$$

Multiplying (A3) by $1/g$, adding the result to (A4), and then using the orthonormality relation (A2), (19) is obtained, confirming the validity of the transform pair (19) and (20).

To prove that all the eigenvalues of the problem (21–23) are positive, we multiply (21) by $\mathcal{Z}_m(z)$ to obtain

$$\frac{N^2\mathcal{Z}_m^2}{gh_m}+\frac{d}{dz}\left(\mathcal{Z}_m\frac{d\mathcal{Z}_m}{dz}\right)=\left(\frac{d\mathcal{Z}_m}{dz}\right)^2+\left(\frac{\mathcal{Z}_m}{2H}\right)^2. \tag{A5}$$

Integrating (A5) over z and making use of the boundary conditions (22) and (23) results in

$$\frac{1}{h_m}\left\{\frac{1}{g}\int_0^{z_T}\mathcal{Z}_m^2(z)N^2(z)dz+\mathcal{Z}_m^2(0)\right\} \quad =\int_0^{z_T}\left\{\left(\frac{d\mathcal{Z}_m(z)}{dz}\right)^2+\left(\frac{\mathcal{Z}_m(z)}{2H}\right)^2\right\}dz+\frac{\mathcal{Z}_m^2(0)}{2H}. \tag{A6}$$

The right-hand side of (A6) is positive. Since $N^2>0$, the term in braces on the left-hand side of (A6) is also positive. Thus, all the eigenvalues are positive, i.e., $h_m>0$ for all m.

To determine if the eigenfunctions $\mathcal{Z}_m(z)$ form a complete set, we first write (19) in the form

$$\hat{\psi}_m(y)=\frac{1}{g}\int_0^{z_T}[1+\delta(z')]\hat{\psi}(y,z')\mathcal{Z}_m(z')N^2(z')dz', \tag{A7}$$

where $\delta(z')$ satisfies

$$\frac{1}{g}\int_0^{z_T}\delta(z')N^2(z')dz'=1. \tag{A8}$$

Using (A7) in (20) results in

$$\hat{\psi}(y,z)=\frac{1}{g}\int_0^{z_T}\left\{[1+\delta(z')]\sum_{m=0}^{\infty}\mathcal{Z}_m(z)\mathcal{Z}_m(z')\right\}\hat{\psi}(y,z')N^2(z')dz'. \tag{A9}$$

The right-hand side of (A9) evaluates to $\hat{\psi}(y,z)$ if

$$[1+\delta(z')]\sum_{m=0}^{\infty}\mathcal{Z}_m(z')\mathcal{Z}_m(z)=\delta(z'-z), \tag{A10}$$

which is the completeness relation. Although a general proof of (A10) is not given, it is confirmed numerically for the special case of constant N in Appendix B. For further discussion, see *Arfken and Weber* [1985, section 8.4] and *Courant and Hilbert* [1953, section 6.3].

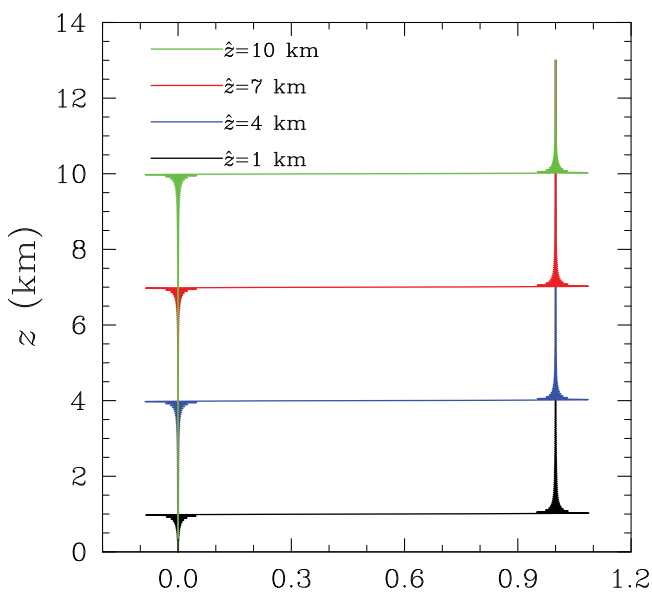

Figure A1. Four plots of the left-hand side of (B15) for the choices $\hat{z}=1$km (black), $\hat{z}=4$km (blue), $\hat{z}=7$km (red), and $\hat{z}=10$ km (green). The two sums on the left-hand side of (B15) have been truncated at $m=500$. These plots, and others with different truncations, demonstrate that the left-hand side of (B15) converges in the mean to the right-hand side of (B15), thereby confirming the completeness of the basis functions $\mathcal{Z}_m(z)$ for the case of constant N.

Appendix B: Calculation of h_m and $\mathcal{Z}_m(z)$

To solve the Sturm-Liouville problem (21–23), consider the idealized case in which the buoyancy frequency N is a constant given by $N = 1.2 \times 10^{-2}\ \mathrm{s}^{-1}$. The solution of the second-order equation (21) has different forms depending on the eigenvalues h_m. We begin by exploring the possibility that one of the eigenvalues is given by $\hat{h}$, which is defined by $\hat{h}=(2NH)^2/g=4328$ m. The corresponding eigenfunction $\hat{\mathcal{Z}}(z)$ then satisfies $d^2\hat{\mathcal{Z}}/dz^2=0$, in which case the solution satisfying the upper boundary condition (22) is $\hat{\mathcal{Z}}(z)=C(z_T-z)$, where C is a constant. The lower boundary condition is satisfied if $\{1+z_T[(1/H)-(1/\hat{h})]\}C=0$. We assume that the constant z_T is specified in such a way that $z_T \neq [(1/\hat{h})-(1/H)]^{-1}=8731$ m, so that $1+z_T[(1/H)-(1/\hat{h})] \neq 0$ and $C = 0$, meaning that the boundary value problem does not have a nontrivial eigenfunction with corresponding eigenvalue $h_m=\hat{h}$. Below, the two cases are investigated separately: $h_m > \hat{h}$ (Case 1) and $0 < h_m < \hat{h}$ (Case 2). The solutions involve solving a transcendental equation using Newton's iterative method for h_m.

Case 1. If the eigenvalues satisfy $h_m > \hat{h}$, then the equation for $\mathcal{Z}_m(z)$ is

$$\frac{d^2\mathcal{Z}_m(z)}{dz^2}-\frac{\mu_m^2}{z_T^2}\mathcal{Z}_m=0, \tag{B1}$$

where

$$\frac{\mu_m^2}{z_T^2}=\frac{N^2}{g}\left(1\hat{h}-\frac{1}{h_m}\right)>0. \tag{B2}$$

In this case, the vertical structure functions satisfying the upper boundary condition are

$$\mathcal{Z}_m(z)=A_m \sinh\left[\mu_m(1-z/z_T)\right], \tag{B3}$$

where A_m is the normalization factor. Through application of the lower boundary condition (23), it can be shown that μ_m is the solution of

$$\tanh(\mu_m)=\frac{\mu_m}{(z_T/\hat{h})[1-\hat{h}/2H-(2H\mu_m/z_T)^2]}. \tag{B4}$$

The transcendental equation (B4) has only one solution, denoted by μ_0 and having the value $\mu_0 = 0.4686$. The corresponding eigenvalue h_0 is obtained from (B2), written in the form

$$h_0=\hat{h}\left[1-(2H\mu_0/z_T)^2\right]^{-1}\approx 7075\ \mathrm{m}. \tag{B5}$$

The top line in the orthonormality relation (A2) is satisfied if the normalization factor is given by

$$A_0=\left\{\frac{N^2 z_T}{2g}\left[\frac{\sinh(\mu_0)\cosh(\mu_0)}{\mu_0}-1\right]+\sinh^2(\mu_0)\right\}^{-1/2}. \tag{B6}$$

Case 2. If the eigenvalues lie in the range $0 < h_m < \hat{h}$, then the equation for $\mathcal{Z}_m(z)$ is

$$\frac{d^2\mathcal{Z}_m(z)}{dz^2}+\frac{\nu_m^2}{z_T^2}\mathcal{Z}_m=0, \tag{B7}$$

where

$$\frac{\nu_m^2}{z_T^2}=\frac{N^2}{g}\left(\frac{1}{h_m}-1\hat{h}\right)>0. \tag{B8}$$

In this case, the vertical structure functions satisfying the upper boundary condition are

$$\mathcal{Z}_m(z)=B_m\sin\left[\nu_m(1-z/z_T)\right], \tag{B9}$$

where B_m is the normalization factor. Through application of the lower boundary condition (23), it can be shown that ν_m is the solution of

$$\tan(\nu_m)=\frac{\nu_m}{(z_T/\hat{h})[1-\hat{h}/2H+(2H\nu_m/z_T)^2]}. \tag{B10}$$

After the transcendental equation (B10) is solved for ν_m, the eigenvalues h_m can be obtained from (B8), written in the form

$$h_m=\hat{h}\left[1+(2H\nu_m/z_T)^2\right]^{-1}\approx\hat{h}\left[1+(2Hm\pi/z_T)^2\right]^{-1}. \tag{B11}$$

The second (approximate) equality follows from the fact that the solutions of the transcendental equation (B10) are approximately $\nu_m\approx m\pi$ for $m=1, 2,\cdots$, with the accuracy of the estimate improving as m increases. The exact and approximate eigenvalues are listed in Table 1. Finally, the top line in the orthonormality relation (A2) is satisfied if the normalization factor is given by

$$B_m=\left\{\frac{N^2z_T}{2g}\left[1-\frac{\sin(\nu_m)\cos(\nu_m)}{\nu_m}\right]+\sin^2(\nu_m)\right\}^{-1/2}. \tag{B12}$$

Note that the dependence of the normalization factors B_m on m is weak because $\nu_m\approx m\pi$, making the $\sin(\nu_m)$ terms in (B12) negligible, which leads to $B_m\approx[2g/(N^2z_T)]^{1/2}\approx 3.2$.

To summarize, the eigenvalue for the external mode is given by (B5) where μ_0 is the single solution of the transcendental equation (B4), while the eigenvalues for the internal modes are given by (B11) where ν_m are the solutions of the transcendental equation (B10). The corresponding eigenfunctions are

$$\mathcal{Z}_m(z)=\begin{cases}A_0\sinh\left[\mu_0(1-z/z_T)\right] & m=0\\ B_m\sin\left[\nu_m(1-z/z_T)\right] & m\geq 1,\end{cases} \tag{B13}$$

where the normalization factors are given by (B6) and (B12). The first five eigenvalues h_m ($m=0, 1, 2, 3, 4$) are listed in Table 1, while the corresponding eigenfunctions are plotted in Figure 2.

To numerically confirm the completeness relation (A10) for the case of constant N, first we write it in the form

$$[1+\delta(z')]\mathcal{Z}_0(z')\mathcal{Z}_0(\hat{z})+[1+\delta(z')]\sum_{m=1}^{\infty}\mathcal{Z}_m(z')\mathcal{Z}_m(\hat{z})=\delta(z'-\hat{z}), \tag{B14}$$

where, for notational convenience, $\hat{z}$ replaces z. The numerical confirmation of (B14) is simpler if (B14) is converted to an integrated form because then the two delta functions will not appear. Thus, integrating (B14) over z' from zero to z, making use of (B13), and finally multiplying by N^2/g results in

$$\begin{aligned}&\frac{A_0N^2z_T}{g\mu_0}\mathcal{Z}_0(\hat{z})\{\cosh(\mu_0)-\cosh\left[\mu_0(1-z/z_T)\right]\}\\&+\sum_{m=1}^{\infty}\frac{B_mN^2z_T}{g\nu_m}\mathcal{Z}_m(\hat{z})\{\cos\left[\nu_m(1-z/z_T)\right]-\cos(\nu_m)\}+\sum_{m=0}^{\infty}\mathcal{Z}_m(0)\mathcal{Z}_m(\hat{z})=\begin{cases}1 & \text{if } z>\hat{z}\\ 0 & \text{if } z<\hat{z}.\end{cases}\end{aligned} \tag{B15}$$

Figure A1 shows plots of the left-hand side of (B15) when $\hat{z}=1, 4, 7, 10$ km and when 500 terms are used in the summation over m. Plots similar to Figure A1, but for different truncations of the sums,

confirm that, although the Gibbs phenomenon occurs near $z=\hat{z}$, the left-hand side of (B15) converges (in the mean) to the unit step function as the number of terms is increased. This is numerical confirmation that (B14) is valid and therefore that the basis functions (B13) form a complete set in the special case of constant N.

Acknowledgments
We would like to thank Wayne Schubert, Paul Ciesielski, Thomas Birner, Mark DeMaria, Eric Maloney, David Randall, Chris Slocum, Rick Taft, Sue van den Heever, and Scott Fulton for their advice. We also would like to thank two anonymous reviewers for comments that improved aspects of the paper. Research support for the first author has been provided by the National Science Foundation under grants ATM-0837932 and AGS-1250966, and under the Science and Technology Center for Multi-Scale Modeling of Atmospheric Processes, managed by Colorado State University through cooperative agreement ATM-0425247. Research support for the second author has been provided by the University of Costa Rica, fellowship OAICE-01-CB-001–2005. The calculations were made on high-end Linux workstations generously provided through a gift from the Hewlett-Packard Corporation.

References

Arfken, G. B., and H. J. Weber (1985), *Mathematical Methods for Physicists*, 832 pp., Academic, Fla, Orlando, Florida.
Back, L. E., and C. S. Bretherton (2009), On the relationship between SST gradients, boundary layer winds and convergence over the tropical oceans, *J. Clim.*, *22*, 4182–4196. doi: 10.1175/2009JCLI2392.1
Charney, J. G., and M. E. Stern (1962), On the stability of internal baroclinic jets in a rotating atmosphere, *J. Atmos. Sci.*, *19*, 159–172. doi: 10.1175/1520-0469(1962)019<0159:OTSOIB>2.0.CO;2.
Courant, R., and D. Hilbert (1953), *Methods of Mathematical Physics*, vol. *1*, 560 pp., Interscience, New York.
Eliassen, A. (1951), Slow thermally or frictionally controlled meridional circulations in a circular vortex, *Astrophys. Norv.*, *5*, 19–60.
Fulton, S. R. (1980), Geostrophic adjustment in a stratified atmosphere, MS thesis, Dep. Atmos. Sci., Colo. State Univ., Fort Collins, Colo.
Fulton, S. R., and W. H. Schubert (1985), Vertical normal mode transforms: Theory and application, *Mon. Weather Rev.*, *113*, 647–658. doi: 10.1175/1520-0493(1985)113<0647:VNMTTA>2.0.CO;2.
Hack, J. J., and W. H. Schubert (1990), Some dynamical properties of idealized thermally-forced meridional circulations in the tropics, *Meteorol. Atmos. Phys.*, *44*, 101–117. doi: 10.1007/BF01026813.
Hack, J. J., W. H. Schubert, D. E. Stevens, and H.-C. Kuo (1989), Response of the Hadley circulation to convective forcing in the ITCZ, *J. Atmos. Sci.*, *46*, 2957–2973. doi: 10.1175/1520-0469(1989)046<2957:ROTHCT>2.0.CO;2.
Haynes, P. H., and T. G. Shepherd (1989), The importance of surface pressure changes in the response of the atmosphere to zonally-symmetric thermal and mechanical forcing, *Q. J. R. Meteorol. Soc.*, *115*, 1181–1208. doi: 10.1002/qj.49711549002.
Held, I. M., and A. Y. Hou (1980), Nonlinear axially symmetric circulations in a nearly inviscid atmosphere, *J. Atmos. Sci.*, *37*, 515–533. doi: 10.1175/1520-0469(1980)037<0515:NASCIA>2.0.CO;2.
Holton, J. R., J. M. Wallace, and J. A. Young (1971), On boundary layer dynamics and the ITCZ, *J. Atmos. Sci.*, *28*, 275–280. doi: 10.1175/1520-0469(1971)028<0275:OBLDAT>2.0.CO;2.
Hou, A. Y., and R. S. Lindzen (1992), The influence of concentrated heating on the Hadley circulation, *J. Atmos. Sci.*, *49*, 1233–1241. doi: 10.1175/1520-0469(1992)049<1233:TIOCHO>2.0.CO;2.
Lindzen, R. S., and A. Y. Hou (1988), Hadley circulations for zonally averaged heating centered off the equator, *J. Atmos. Sci.*, *45*, 2416–2427. doi: 10.1175/1520-0469(1988)045<2416:HCFZAH>2.0.CO;2.
Ling, J., and C. Zhang (2013), Diabatic heating profiles in recent global analyses, *J. Clim.*, *23*, 3307–3325. doi: 10.1175/JCLI-D-12-00384.1.
Nieto Ferreira, R., and W. H. Schubert (1997), Barotropic aspects of ITCZ breakdown, *J. Atmos. Sci.*, *54*, 251–285. doi: 10.1175/1520-0469(1997)054<0261:BAOIB>2.0.CO;2.
Nolan, D. S., C. Zhang, and S.-H. Chen (2007), Dynamics of the shallow meridional circulation around Intertropical Convergence Zones, *J. Atmos. Sci.*, *64*, 2262–2285. doi: 10.1175/JAS3964.1.
Nolan, D. S., S. W. Powell, C. Zhang, and B. E. Mapes (2010), Idealized simulations of the Intertropical Convergence Zone and its multilevel flows, *J. Atmos. Sci.*, *67*, 4028–4053. doi: 10.1175/2010JAS3417.1.
Schneider, E. K., and R. S. Lindzen (1977), Axially symmetric steady-state models of the basic state for instability and climate studies. Part I. Linearized calculations, *J. Atmos. Sci.*, *34*, 263–279. doi: 10.1175/1520-0469(1977)034<0263:ASSSMO>2.0.CO;2.
Schubert, W. H., and B. D. McNoldy (2010), Application of the concepts of Rossby length and Rossby depth to tropical cyclone dynamics, *J. Adv. Model. Earth Syst.*, *2*, 13, doi:10.3894/JAMES.2010.2.7.
Schubert, W. H., P. E. Ciesielski, D. E. Stevens, and H.-C. Kuo (1991), Potential vorticity modeling of the ITCZ and the Hadley circulation, *J. Atmos. Sci.*, *48*, 1493–1509. doi: 10.1175/1520-0469(1991)048<1493:PVMOTI>2.0.CO;2.
Stevens, B., J. Duan, J. C. McWilliams, M. Münnich, and J. D. Neelin (2002), Entrainment, Rayleigh friction, and boundary layer winds over the tropical Pacific, *J. Clim.*, *15*, 30–44. doi: 10.1175/1520-0442(2002)015<0030:ERFABL>2.0.CO;2.
Takayabu, Y. N., S. Shige, W.-K. Tao, and N. Hirota (2010), Shallow and deep latent heating modes over tropical oceans observed with TRMM PR spectral latent heating data, *J. Clim.*, *23*, 2030–2046. doi: 10.1175/2009JCLI3110.1.
Tomas, R. A., and P. J. Webster (1997), The role of inertial instability in determining the location and strength of near-equatorial convection, *Q. J. R. Meteorol. Soc.*, *123*, 1445–1482. doi: 10.1002/qj.49712354202.
Trenberth, K. E., D. P. Stepaniak, and J. M. Caron (2000), The global monsoon as seen through the divergent atmospheric circulation, *J. Clim.*, *13*, 3969–3993. doi: 10.1175/1520-0442(2000)013<3969:TGMAST>2.0.CO;2.
Wang, B., and H. Rui (1990), Dynamics of the coupled moist Kelvin-Rossby wave on an equatorial β-plane, *J. Atmos. Sci.*, *47*, 397–413. doi: 10.1175/1520-0469(1990)047<0397:DOTCMK>2.0.CO;2.
Wang, C.-C., and G. Magnusdottir (2005), ITCZ breakdown in three-dimensional flows, *J. Atmos. Sci.*, *62*, 1497–1512. doi: 10.1175/JAS3409.1.
Wu, Z., E. S. Sarachik, and D. S. Battisti (2000), Vertical structure of convective heating and the three-dimensional structure of the forced circulation on an equatorial beta plane, *J. Atmos. Sci.*, *57*, 2169–2187. doi: 10.1175/1520-0469(2000)057<2169:VSOCHA>2.0.CO;2.
Yin, B., and B. A. Albrecht (2000), Spatial variability of atmospheric boundary layer structure over the eastern equatorial Pacific, *J. Clim.*, *13*, 1574–1592. doi: 10.1175/1520-0442(2000)013<1574:SVOABL>2.0.CO;2
Zhang, C., and S. M. Hagos (2009), Bi-modal structure and variability of large-scale diabatic heating in the tropics, *J. Atmos. Sci.*, *66*, 3621–3640. doi: 10.1175/2009JAS3089.1.
Zhang, C., M. McGauley, and N. A. Bond (2004), Shallow meridional circulation in the tropical eastern Pacific, *J. Clim.*, *17*, 133–139. doi: 10.1175/1520-0442(2004)017<0133:SMCITT>2.0.CO;2.
Zhang, C., D. S. Nolan, C. D. Thorncroft, and H. Nguyen (2008), Shallow meridional circulations in the tropical atmosphere, *J. Clim.*, *21*, 3453–3470. doi: 10.1175/2007JCLI1870.1.

